JGR Solid Earth

Key Points:

- Matrix porosity and permeability of basalts spilitized at 200–440°C are similar to values of fresh and clay/zeolite-altered basalts
- Interpillow hyaloclastites are the most permeable upper crustal rocks $\leq 10^{-15}$ m²; epidosites have similar/higher permeabilities $\leq 10^{-14}$ m²
- Upscaled matrix permeability of spilitized lavas ($\sim 10^{-16}$ m²) meets minimum requirement for observed heat and fluid flow at the seafloor

Author Contributions:

Conceptualization: Alannah C. Brett-Adams, Larryn W. Diamond, Samuel A. Gilgen
Formal analysis: Alannah C. Brett-Adams, Samuel Weber
Funding acquisition: Larryn W. Diamond
Investigation: Alannah C. Brett-Adams, Samuel A. Gilgen
Methodology: Alannah C. Brett-Adams, Larryn W. Diamond, Samuel Weber

Rock-Matrix Porosity and Permeability of the Hydrothermally Altered, Upper Oceanic Crust, Oman Ophiolite

Alannah C. Brett-Adams[1] , **Larryn W. Diamond[1]** , **Samuel Weber[1]** , **and Samuel A. Gilgen[1]**

[1]Institute of Geological Sciences, University of Bern, Bern, Switzerland

Abstract Porosity and permeability are key controls on hydrothermal circulation and alteration in magmatically heated upper oceanic crust. However, the hydraulic properties of basalts altered above 200°C are largely unknown, leaving their role in high-temperature systems unclear. Here, we assess rock-matrix porosities and permeabilities of pervasively altered MORB-like basalts from outcrops in the sheeted dikes and axial lavas of the Semail ophiolite, Oman. The samples represent regional spilite alteration (chlorite–albite–quartz $\pm$ actinolite; 150–440°C) and localized epidosite alteration (epidote–quartz; 255–435°C). Porosity and permeability of spilitized rocks vary as follows: interpillow hyaloclastites (14–27 vol.%, 10^{-17}–10^{-15} m²) > pillow cores (4–12 vol.%; $\sim 10^{-19}$–6×10^{-18} m²) > pillow rims (4–11 vol.%; $\sim 10^{-19}$–2×10^{-18} m²) > massive sheet flows (1–9 vol.%; $\sim 10^{-19}$ m²) $\geq$ dikes (1–5 vol.%; $\sim 10^{-19}$ m²). Pillow values fall within the ranges of existing data on fresh and low-temperature altered basalts in in situ crust. However, hyaloclastite permeabilities are 1–4 orders of magnitude higher and are clearly preferred flow paths. Epidosites have elevated porosity and permeability irrespective of rock morphology (18–26 vol.%; $\sim 10^{-16}$–10^{-14} m²). Pillow stacks have upscaled ($\sim 10^4$ m³) matrix porosities and permeabilities of ~ 9 vol.% and $\sim 10^{-17}$–10^{-16} m² when spilitized and 16 vol.% and up to $\sim 10^{-14}$ m² when epidotized. Upscaled permeabilities of spilites meet minimum requirements for observed heat and fluid discharge from high-temperature seafloor systems even without fracture networks, and reflect strong flow through the rock-matrix.

Plain Language Summary The ocean crust makes up $\sim 70\%$ of the earth's surface and pathways for fluid flow through this crust control its exchange of heat and chemical components with the oceans. Often the upper oceanic crust is thought of as a fractured aquifer but its pervasive replacement by hydrothermal minerals and the formation of metal deposits on the seafloor show that the rock-matrix also serves as an efficient fluid pathway. To complement existing porosity and permeability data on fresh and low temperature altered basalts, we provide new measurements of the rock-matrix of basalts in a slice of oceanic crust that was pervasively altered at ~ 200–440°C by hydrothermal fluids and then exhumed in Oman. Based on these laboratory measurements, estimates are provided of the hydraulic properties of the upper oceanic crust at 10^4 m³ scale. These results demonstrate the importance of the high-temperature altered rock-matrix as a water conductor in the oceanic crust. The new values reach the minimum permeability required to explain observed heat and fluid discharge near actively spreading tectonic plate margins on the seafloor, even without considering fracture networks.

1. Introduction

Understanding hydrothermal transport of solutes and heat through the basaltic, upper oceanic crust requires a quantitative and realistic model of crustal permeability (Alt, 1995; Coogan & Gillis, 2018; Fisher, 1998; Hasenclever et al., 2014). Numerical simulations of oceanic hydrothermal systems have invoked high bulk permeabilities in the upper crust (10^{-16}–10^{-9} m²; Fisher, 1998 and references therein; Hasenclever et al., 2014; Price et al., 2022) to explain observed heat and fluid discharge fluxes at the seafloor. These high values contrast with the 10^{-21}–10^{-16} m² range of measured rock-matrix permeabilities, which only partly overlap with the 10^{-18}–10^{-10} m² results from in situ hydraulic tests (e.g., Anderson et al., 1985; Becker, 1989; Becker & Davis, 2003; Becker & Fisher, 2000; Davis & Becker, 2002; Fisher, 1998). The implication is that fracture networks dominate permeability, and indeed studies of such networks have yielded very high to extremely high values of $\sim 10^{-12}$–10^{-6} m² (Nehlig, 1994; van Everdingen, 1995).

A closer examination of available permeability estimates raises questions about their applicability to the portions of the upper oceanic crust undergoing hydrothermal alteration at prehnite–pumpellyite to greenschist facies

Project Administration: Larryn W. Diamond
Supervision: Larryn W. Diamond
Validation: Alannah C. Brett-Adams, Samuel Weber
Visualization: Alannah C. Brett-Adams
Writing – original draft: Alannah C. Brett-Adams
Writing – review & editing: Alannah C. Brett-Adams, Larryn W. Diamond

conditions (∼150–500°C). On the one hand, it is recognized that fracture permeability may have been overestimated because individual fractures have been modeled as parallel plates with infinite extents (Fisher, 1998; van Everdingen, 1995). On the other hand, the apparent dominance of fracture permeability is somewhat at odds with the evidence for intense, pervasive alteration of the rock matrix of the upper crust, which testifies to widespread metasomatism and scavenging of metals by hydrothermal fluids, ultimately leading to formation of seafloor volcanogenic massive sulfide (VMS) deposits (Hannington, 2014; Jowitt et al., 2012; Patten et al., 2016; Richardson et al., 1987; Richter & Diamond, 2022). Previous measurements of rock-matrix permeability have been made mainly on fresh glassy basalts and on basalts altered to clays at low temperatures (below ∼150°C). In contrast, the matrix permeability of the vast quantities of basalts altered at higher temperatures is largely unquantified at the cm^3 scale, and no upscaled values are available for larger bodies of rock. Thus, the hydraulic role of the rock matrix in controlling fluid convection through the high-temperature altered upper crust is ambiguous.

To fill these gaps in knowledge, the present study provides new laboratory measurements of rock-matrix porosity and permeability of pervasively altered basalts from outcrops of the MORB-type lavas and comagmatic sheeted dike complex (SDC) in the Semail ophiolite, Oman. Two mineralogical types of alteration are examined: spilites consisting of albite + chlorite ± actinolite + relict augite, which are volumetrically most important; and epidosites consisting of epidote + quartz + Fe-oxide, which are apparently rare in in situ oceanic crust but are common in Archean greenstones and in Phanerozoic ophiolites such as Semail (Alabaster & Pearce, 1985; Coelho et al., 2015; Galley et al., 1993; Gilgen et al., 2014; Gillis & Banerjee, 2000; Hannington et al., 2003; Richardson et al., 1987). Measurements at the drill-core (∼15 cm^3) scale are corrected for post-alteration effects, and upscaled values for entire pillow stacks at the 10^4 m^3 scale are obtained from the weighted volumetric contributions of their constituent rock types. Our findings quantify the porosity and permeability that led to the huge volumes of pervasive prehnite–pumpellyite to greenschist facies alteration in the Semail upper crust (Belgrano et al., 2022). The values also explain visible patterns of alteration intensity in epidosite zones and they demonstrate the importance of interpillow hyaloclastites as permeable conduits through the volcanic sequence. The final upscaled results are suitable for use in thermal-hydraulic-chemical simulations of sub-seafloor hydrothermal processes.

2. Geological Setting and Hydrothermal Alteration of the Semail Ophiolite

2.1. Geological Setting

The Semail ophiolite represents a slice of oceanic lithosphere that formed above a nascent subduction zone, most likely in a proto-arc setting, during the Upper Cretaceous (Belgrano & Diamond, 2019; Guilmette et al., 2018; MacLeod et al., 2013; Pearce et al., 1984). The magmatism that generated the Semail crust occurred along a fast-spreading ridge axis at 96.1–95.6 Ma (Rioux et al., 2021), producing gabbros, a sheeted dike complex (SDC) and overlying comagmatic basalt to basaltic-andesite lavas (Figure 1a). These lavas, known as the Geotimes or V1 unit, have MORB-like basalt to basaltic-andesite character and are locally H_2O-enriched (e.g., MacLeod et al., 2013). Despite the suprasubduction zone setting of the Semail axial upper crust, its lava morphologies, igneous stratigraphy and structural characteristics are comparable to those of modern, fast-spreading mid-ocean ridges, such as the East Pacific Rise (e.g., Einaudi et al., 2000; Kusano et al., 2014; Nicolas et al., 2000). Owing to these similarities, the axial Semail SDC and Geotimes lavas are the focus of our study.

Overlying the Semail axial units is a prominent layer of metalliferous sediments, which marks a pause in volcanism, followed by a thick sequence of younger lavas that have no recognized coeval sheeted dike complex but seem instead to have been fed by localized dike swarms (Figure 1b). These post-axial lavas (also known as V2) are almost as voluminous as the combined axial SDC and Geotimes lavas (Belgrano et al., 2019). They include off-axis primitive basalts of the Lasail unit overlain by post-axial island-arc tholeiites (Tholeiitic Alley unit) and boninites locally up to 2 km thick (Boninitic Alley unit; Belgrano et al., 2019). All these lavas were emplaced at 95.6–95.2 Ma (Rioux et al., 2021), directly after the axial Geotimes lavas. Thus, the entire Semail crust was formed within about 0.9 Ma (Rioux et al., 2021) without a radiometrically resolvable hiatus between its axial and post-axial igneous activity.

2.2. Hydrothermal Alteration

The Semail SDC is regionally altered to albite + actinolite + chlorite spilite assemblages (Belgrano et al., 2022; Nehlig et al., 1994), with most dikes showing pervasive alteration in which augite is the only igneous relict.
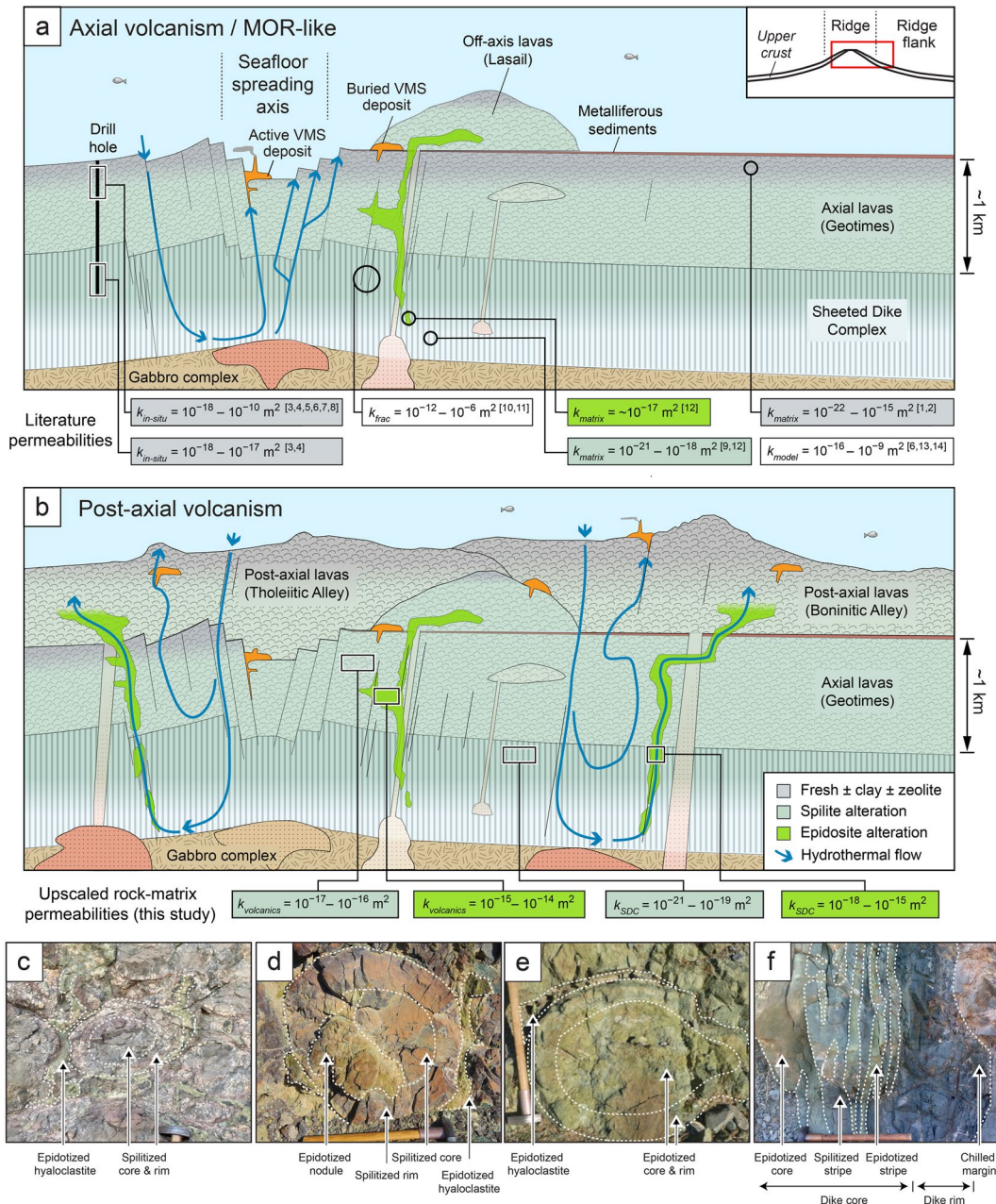
Figure 1. Schematic cross-sections through the Semail upper oceanic crust at two stages of its development, showing regional alteration patterns, previously published permeability data, new upscaled rock-matrix data from this study and field photographs of spilite and epidosite alteration in lavas and dikes (modified after Brett-Adams et al. (2021) and Gilgen et al. (2016)). (a) MOR-type axial spreading stage, with spilite alteration of the axial Geotimes lavas, comagmatic SDC and off-axis Lasail lavas. Also axial volcanogenic massive sulfide (VMS) deposits and rare epidosite alteration are shown. Labeled literature permeability ranges are from various locations but are overlain on the Semail axial setting and summarize: bulk permeability from MOR in situ hydraulic tests ($k_{in\ situ}$), rock-matrix permeability (k_{matrix}) from MOR, Troodos and Semail ophiolites, permeability modeled using ophiolite fracture maps (k_{frac}) from Semail and Troodos ophiolites, and permeability invoked for heat and fluid flux models (k_{model}) from: [1]Johnson (1980b), [2]Jarrard et al. (2003), [3]Anderson et al. (1985), [4]Becker (1989), [5]Becker and Fisher (2000), [6]Fisher (1998), [7]Becker and Davis (2003), [8]Davis and Becker (2002), [9]Brett-Adams et al. (2021) [10]van Everdingen (1995), [11]Nehlig (1994), [12]Coelho et al. (2015), [13]Hasenclever et al. (2014), [14]Price et al. (2022). (b) Post axial magmatic stage showing burial of the Geotimes and Lasail lavas by Tholeiitic Alley and Boninitic Alley lavas fed by dike swarms. Spilite alteration is ubiquitous except for the uppermost lavas altered to clay and zeolites. Large km-wide epidosite bodies locally overprint spilite alteration. Permeability values from this study denote ranges of anisotropy in upscaled volumes of rock (~10^4 m^3). (c) Incipient epidosite in pillow lava, in which only the interpillow hyaloclastite zone is epidotized, whereas the pillow core and rim zones retain precursor epidote-free spilite alteration. (d) Intermediate epidosite in pillow lavas, in which interpillow hyaloclastite and part of pillow core are altered to epidosite. (e) Complete epidosite in pillow lava. None of the pillows in images c–e display cooling joints. (f) Stripy intermediate epidosite alteration of core of a spilite dike. Gray stripes in core and chilled margin show spilite alteration.

Weakly altered dikes are rare (Miyashita et al., 2003). The Geotimes and Lasail lavas are also pervasively altered to spilite assemblages throughout the ophiolite, characterized by albite + chlorite ± actinolite ± relict augite (Alabaster & Pearce, 1985; Alabaster et al., 1982; Belgrano et al., 2022), with glass preserved only very rarely (Kusano et al., 2017). The above alteration is estimated to have occurred at temperatures of ∼200–440°C at near-hydrostatic fluid pressures of >31–54 MPa (taking into account a seafloor depth of ∼3,100–3,500 m b.s.l.; Belgrano et al., 2021), at a range of depths up to 2,050 m below seafloor (Richter & Diamond, 2022). The post-axial Tholeiitic Alley and Boninitic Alley lavas are regionally altered mostly to smectite + albite with pore-fillings of zeolite and celadonite. However, spilite assemblages identical to those in the underlying Geotimes lavas are also developed at the base of the Tholeiitic and Boninitic Alley units and locally higher up in the stratigraphy near swarms of sills or dikes (Figure 1b; Alabaster & Pearce, 1985; Belgrano et al., 2022). No direct radiometric ages are available for the spilite alteration minerals. We assume that the spilitization occurred throughout the 0.9 Ma duration of axial and post-axial magmatic activity.

Pervasive epidosite alteration makes up just a few percent of the exposed area of the Semail upper crust (Belgrano et al., 2022). Individual bodies reach up to 1 km² in outcrop extent, replacing earlier spilite alteration in the SDC and in all overlying lavas, most commonly in the Geotimes and Lasail units (Gilgen et al., 2016). Epidosites in the Semail SDC are much smaller and less numerous than those in the lava sequence (Gilgen et al., 2016), opposite to the situation in the well-known Troodos ophiolite in Cyprus (Richardson et al., 1987). Fluid inclusion evidence shows that epidotization occurred at 255–435°C, at near-hydrostatic fluid pressures of 35–68 MPa (Richter & Diamond, 2022). Epidosite alteration of cross-cutting dikes of known volcanostratigraphic affinity demonstrates that the large majority of epidosites formed during post-axial volcanism, with the remainder during earlier off-axis Lasail and possibly Geotimes volcanism (Gilgen et al., 2016).

Each major epidosite occurrence in Geotimes pillow lavas consists of three concentric alteration zones corresponding to stages in the progressive transformation of spilite to epidosite (Gilgen et al., 2016; Weber et al., 2021): (a) a peripheral zone of *incipient epidosite* up to 100–200 m wide, in which only the interpillow hyaloclastite is converted to epidosite, leaving a spilite assemblage in the pillow cores and rims (Figure 1c); (b) a medial zone of *intermediate epidosite* also up to 200 m wide, in which the interpillow hyaloclastite and pillow cores are converted to epidosite, while pillow rims retain spilite alteration (Figure 1d); and (c) a patchy central zone of *complete epidosite* up to 300 m wide and 1.5 km long, in which interpillows, pillow cores and pillow rims are all converted to epidosite (Figure 1e). Although epidosites mapped as *complete* exhibit an intense pistachio-green color in outcrop owing to their high epidote content, they mostly still contain minor relict augite and/or chlorite and are only rarely mineralogical endmembers with 100 vol.% quartz + epidote + titanite + Fe-oxides (Weber et al., 2021). Even where Geotimes pillow lavas are completely epidotized, interlayered massive sheet flows are only weakly altered, displaying epidosite along the margins of joints or along the centers of cooling columns, rarely summing to more than 10 vol.% epidosite at the outcrop scale, the remainder being preserved spilite alteration. Epidosites in the SDC are typically manifested by alteration stripes a few cm wide within and parallel to individual dikes (Figure 1f; Gilgen et al., 2016), similar to that in the Troodos ophiolite (Cann et al., 2014). Collectively, the above field relationships showing overprinting of spilites by epidosites are a clear message from nature that the rock-matrix permeabilities (*k*) of the spilites follow the relative order:

$$k_{\text{hyaloclastite}} > k_{\text{pillow cores}} > k_{\text{pillow rims}} > k_{\text{massive flows}} \geq k_{\text{dikes}} \tag{1}$$

Any quantitative measurements of spilite rock-matrix permeability are therefore expected to reflect this order.

2.3. Macroscopic Fractures and Veins

Major faults flanked by fracture networks occur at approximately kilometer frequency in the Semail upper crust (e.g., Belgrano et al., 2019). At the outcrop scale, cooling joints and other spaced fractures are prominent in the SDC (Nehlig, 1994), and columnar cooling joints are common in Geotimes massive sheet flows. Most outcrops of Geotimes pillow lavas have surprisingly few cooling joints, as demonstrated by the rarity of fracture coatings of epidote and other high-*T* minerals even in strongly epidotized outcrops (e.g., Figures 1c–1e). Only a minority of outcrops display abundant radial cooling joints in pillow interiors (often coated by prehnite) and corresponding tortoise-shell patterns on pillow exteriors (e.g., Figure 2a). It is not clear why some Geotimes outcrops have cooling joints and others not, but in any case they appear to be only of local importance. In contrast, pillows of the off-axis Lasail unit ubiquitously contain cooling joints, typically entirely filled by epidote + quartz
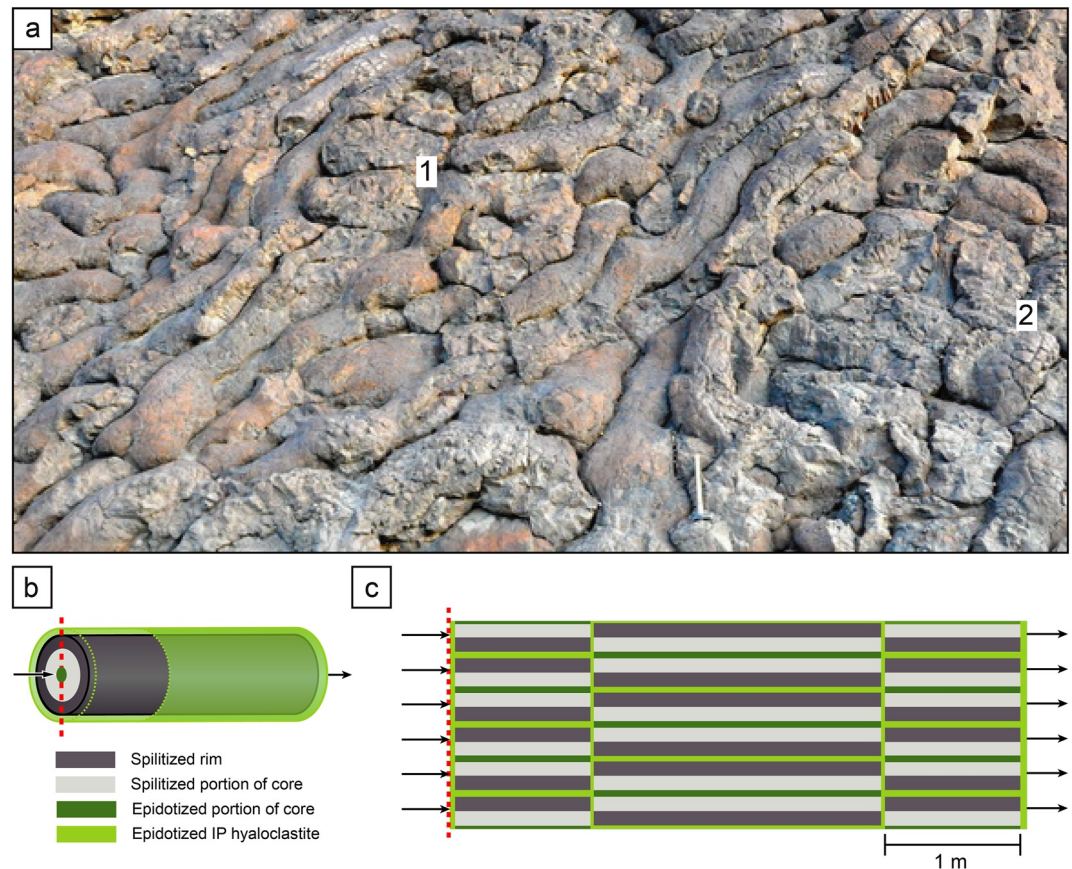
Figure 2. (a) Outcrop of pillow lavas in ridge-axial Geotimes Unit at type locality in Wadi Jizzi, demonstrating tubular shape of individual pillows (hammer is 60 cm long). Radial columnar cooling joints (1, 2) are abundant, in contrast to the pillows in Figures 1c–1e. (b) Simplified 3D geometry of a pillow showing intermediate-stage epidotization, with cores, rims and interpillow (IP) hyaloclastites of different isotropic permeabilities, as used for hydraulic simulations (arrows show fluid flow direction). (c) Model pillow stack in 2D section parallel to long axes of pillow tubes, showing seven whole-width and four half-width pillows. Legend as in (b).

wherever the adjacent rock matrix is epidotized. Although all of the above macroscopic fracture types undoubtedly facilitate hydrothermal circulation, their quantitative role is outside the scope of the present investigation.

In addition to sub-seafloor spilite and epidosite alteration, the SDC and Geotimes units also show later features of importance to our study. First, hydrothermal veins of coarsely crystalline calcite are common, often bordered by haloes in which calcite fills adjacent rock pores. These veins cross-cut and hence postdate all other vein types in the ophiolite (Richter & Diamond, 2022). They formed at ~70–90°C from waters with 0.2–0.7 wt.% $NaCl_{equiv.}$, well below the ~3.2 wt.% $NaCl_{equiv.}$ seawater-like salinity of the hydrothermal fluids that caused the spilite and epidosite alteration (Richter & Diamond, 2022). Second, open fractures induced during obduction and subaerial weathering are ubiquitous and abundant. Third, many of these fractures are coated by fine-grained calcite travertine, which precipitated upon evaporation of shallow groundwaters during exposure of the outcrops. The calcite veins and the travertine are referred to hereafter collectively as "late calcite."

3. Samples

Samples were collected from 10 outcrop localities of the weakly vesicular axial Geotimes lavas and non-vesicular comagmatic SDC in the Semail ophiolite. The samples cover the small variation of vesicularity in these units. Outcrops were chosen with as little post-epidosite hydrothermal calcite veining, wadi travertine, and open fractures as possible. Eighteen samples were retrieved as cylindrical plugs using a portable, water-cooled drill with a diamond-tipped core bit of 2.54 cm diameter. In addition, 30 oversized hand samples were taken where outcrop

conditions allowed extraction by leverage with chisels without heavy hammering, so as to avoid inducing fractures. These large samples were subsequently cored in the laboratory.

Interpillow hyaloclastites altered to epidosite have the same high tenacity as other epidosites and were sampled as above. However, the spilitized hyaloclastites are too fragile to drill and so samples from pillow triple junctions were carefully prized out of the outcrops, wrapped in padding and transported in rigid containers. The thinner layers of hyaloclastite enveloping the remainder of the pillows are too friable to sample and analyze.

All the samples were examined under a 20X hand lens and any showing notable through-going fractures or calcite veins were discarded, leaving only 48 high quality samples for measurement of rock-matrix properties. The characteristics and locations of each sample are summarized in Table 1.

4. Methods

4.1. Bulk-Rock Geochemistry, Mineralogy, and Petrography

Mineral abundances were determined by combining several methods: element mapping of thin-sections by electron microprobe recast into mineral abundances using XMapTools (Lanari et al., 2018); standard powder x-ray diffraction; and calculation of calcite contents from the concentration of carbon determined in a Thermo Scientific FlashSmart™ carbon-nitrogen-sulfur (CNS) elemental analyzer, all at the University of Bern.

Descriptions of pores types, igneous features, alteration mineralogy and textures were made based on petrographic thin-sections viewed in transmitted-light microscopy and in scanning electron microscopy in back-scattered electron mode (BSE-SEM). A Zeiss Evo50 environmental SEM at the University of Bern was used with a 20 kV, 2.5 nA beam at 28 Pa chamber pressure. Mineral identification was aided by Raman microspectroscopy with a Jobin–Yvon LabRam HR800 instrument at the University of Bern.

Major-element concentrations in bulk samples were measured by one of two techniques. Most samples were homogenized into pressed powder pellets and analyzed by laser-ablation inductively coupled plasma mass spectroscopy (LA-ICP-MS) at the University of Bern following the technique of Peters and Pettke (2016). The remaining samples were measured using a PANalytical Axios™ WDS x-ray fluorescence (XRF) instrument at ETH-Zurich with a 20–60 kV, 40–100 mA beam from a rhodium tube using the procedure outlined by Gilgen et al. (2014, 2016).

4.2. Porosity

Connected porosity was measured with an uncertainty of <1 vol.% using a Micromeritics AccuPyc™ 1340 helium-gas pycnometer at the University of Bern. Cylindrical sample plugs (5–23 cm^3) were measured for skeletal volume and density by pycnometer, and for bulk volume by caliper. The skeletal volumes of irregularly shaped and fragile specimens were obtained from density measurements using standard paraffin immersion. All measurements were made at room temperature. Since the masses of the dry bulk and skeletal samples are identical, porosity was calculated by:

$$\phi = 100 - 100\left[\frac{m_{skel}\rho_{bulk}}{m_{bulk}\rho_{skel}}\right] \tag{2}$$

where ϕ is porosity (vol.%), m_{bulk} and m_{skel} are the masses (g) of the bulk and skeletal samples respectively, ρ_{bulk} is dry bulk density (g/cm^3) and ρ_{skel} is skeletal density (g/cm^3). The results for each sample were corrected for pore-clogging by late calcite by adding the sample's volume-fraction of calcite (~0.2–18 vol.%; Table 1) to the pycnometer measurements.

Corrections were then made for fracture porosity as follows. Thin-sections of each sample were imaged in SEM-BSE to evaluate the presence of any microfractures. Six of the 48 imaged thin-sections contain rare or a few open fractures that cross-cut, and hence post-date, the spilite and epidosite alteration minerals. Based on the apertures and semiquantitative abundance of these fractures we estimated the fracture porosities in each of the six sections (0.5–2 vol.%) and subtracted them from the calcite-corrected pycnometer measurements (Table 1).

4.3. Permeability

Permeabilities were measured at CoreLab, Aberdeen using a Core Measurement System CMS™-300 unsteady-state (transient) permeameter with He gas at room temperature (lower detection limit ~9.8 × 10^{-20} m^2).

Table 1
Sample Locations, Alteration Types, and Petrophysical Analyses (This Study)

Sample ID	UTM mE (zone: 40°N)	UTM mN (zone: 40°N)	Igneous rock morphology/textural zone	Alteration type	Epidote + quartz content[a,b] (vol.%)	Porosity raw[c] (vol.%)	Calcite content[d] (vol.%)	Microfracture abundance (relative)[e]	Porosity corrected[f] (vol.%)	Permeability[g] (m²)	Density (g/cm³)
AB17-42F-spl/e-a	432358	2739423	Massive flow	Spilite	33	3.6	5.6	–	9.2	9.87×10^{-20}	2.80
AB17-42F-epi-a	432358	2739423	Massive flow	Epidosite	91	6.1	4.6	0.5	10.2	5.07×10^{-18}	2.93
AB17-31C-spl-b	538351	2608870	Dike	Spilite	18	1.6	0.2	–	1.8	9.87×10^{-20}	2.78
AB17-31C-epi	538351	2608870	Dike	Epidosite	66	8.1	5.8	–	13.9	3.04×10^{-18}	3.00
AB17-32C-spl	538351	2608870	Dike	Spilite	20	4.8	0.4	–	5.2	2.46×10^{-19}	2.81
AB17-32C-epi	538351	2608870	Dike	Epidosite	63	5.0	2.8	–	7.8	1.90×10^{-18}	3.01
AB17-33C-spl	538351	2608870	Dike	Spilite	19	0.6	0.3	–	0.9	9.87×10^{-20}	2.79
AB17-33C-epi	538351	2608870	Dike	Epidosite	61	8.0	0.5	–	8.5	3.43×10^{-17}	2.77
AB17-33R-epi	538351	2608870	Dike	Epidosite	88	9.0	1.6	1.5	9.1	3.98×10^{-15}	3.02
AB17-37C-spl	443641	2715879	Pillow core	Spilite	9	0.6	4.8	–	5.4	9.93×10^{-19}	2.81
AB17-37C-epi-a	443641	2715879	Pillow core	Epidosite	100	15.9	4.1	1.5	18.5	1.91×10^{-15}	2.67
AB17-39C-spl	435338	2725271	Pillow core	Spilite	29	11.4	0.3	–	11.7	6.53×10^{-18}	2.59
AB17-40C-spl-a	435338	2725271	Pillow core	Spilite	30	11.4	0.5	2.0	9.8	7.43×10^{-18}	2.53
AB17-41C-spl-a	432249	2739587	Pillow core	Spilite	17	7.4	9.6	1.5	9.1	6.26×10^{-18}	2.61
AB17-41C-epi-b	432249	2739587	Pillow core	Epidosite	96	7.4	13.1	–	20.5	1.94×10^{-17}	2.86
AB17-44C-spl	432150	2739701	Pillow core	Spilite	25	7.9	1.8	–	9.7	9.87×10^{-20}	2.56
AB17-44R-spl	432150	2739701	Pillow rim	Spilite	16	5.1	0.7	–	5.8	9.87×10^{-20}	2.62
AB17-44C-epi	432150	2739701	Pillow core	Epidosite	100	8.8	17.8	0.5	26.1	1.64×10^{-17}	2.93
AB16-4272c	443182	2716103	Pillow core	Spilite	12	3.3	4.7	–	8.0	9.87×10^{-20}	2.77
AB16-427R	443182	2716103	Pillow rim	Spilite	12	0.6	7.6	–	3.2	9.87×10^{-20}	2.77
AB16-4273c	443182	2716103	Pillow core	Epidosite	72	10.7	3.1	–	13.8	1.32×10^{-16}	2.86
AB17-25C	431934	2739740	Pillow core	Epidosite	81	13.0	0.8	–	13.8	3.51×10^{-16}	2.79
AB16-4431bR-1_A	431979	2739807	Pillow rim	Epidosite	66	9.7	9.0	–	18.7	6.52×10^{-17}	2.91
LD10-120-3	444490	2739546	Pillow core	Epidosite	59	9.4	9.4	–	18.7	4.32×10^{-18}	2.84
AB16-4131C	431926	2739580	Pillow core	Epidosite	79	6.2	2.2	–	8.4	1.89×10^{-18}	3.02
SG14-56	431785	2739627	Pillow core	Epidosite	–	4.1	7.2	–	11.3	9.85×10^{-17}	3.04
LW5C	431950	2740730	Pillow core	Epidosite	–	10.1	0.0	–	10.1	2.92×10^{-15}	2.72
LW7-1P	432080	2739611	Interpillow hyaloclastite	Epidosite	–	10.8	6.3	–	17.1	2.70×10^{-15}	2.78
AB16-4133a	431927	2739580	Interpillow hyaloclastite	Epidosite	–	6.2	11.0	–	17.2	1.31×10^{-17}	3.00
SWOM-1885	432184	2737889	Interpillow hyaloclastite	Epidosite	–	6.8	1.4	–	8.2	4.70×10^{-16}	2.98
RWO1-ST52	434864	2715362	Interpillow hyaloclastite	Epidosite	–	11.0	9.8	–	20.8	–	2.94
SG13-33A	431747	2739254	Massive flow	Spilite	–	0.6	0.6	–	1.2	3.34×10^{-19}	2.89
SG14-43	431747	2739254	Dike	Spilite	–	0.6	3.9	–	4.5	3.90×10^{-19}	2.78

Table 1
Continued

Sample ID	UTM mE (zone: 40°N)	UTM mN (zone: 40°N)	Igneous rock morphology/textural zone	Alteration type	Epidote + quartz content[a,b] (vol.%)	Porosity raw[c] (vol.%)	Calcite content[d] (vol.%)	Microfracture abundance (relative)[e]	Porosity corrected[f] (vol.%)	Permeability[g] (m²)	Density (g/cm³)
AB16-4231	449116	2691867	Pillow rim	Spilite	–	10.2	1.0	–	11.1	6.58×10^{-20}	2.45
SG13-29B	431965	2739360	Pillow core	Spilite	–	7.3	2.1	–	9.4	3.64×10^{-18}	2.67
AB16-4232	449116	2691867	Pillow core	Spilite	–	4.7	2.5	–	7.2	9.87×10^{-20}	2.58
LD10/105	438374	2686042	Pillow rim	Spilite	–	10.1	1.1	–	11.3	2.17×10^{-18}	2.46
AB16-4394T	435337	2725271	Pillow rim	Spilite	–	7.4	1.0	–	8.4	4.63×10^{-19}	2.53
LD10-104-1b	468748	2656024	Pillow core	Spilite	–	9.0	0.2	–	9.2	1.57×10^{-18}	2.60
LD10-104-2c	468748	2656024	Pillow core	Spilite	–	7.2	0.2	–	7.4	1.14×10^{-18}	2.65
LD10-104-3b	468748	2656024	Pillow rim	Spilite	–	5.1	0.2	–	5.3	5.56×10^{-19}	2.68
LD10-104-3c	468748	2656024	Pillow crust	Spilite	–	9.6	0.2	–	9.8	–	2.60
LD10-145-2	449105	2691860	Interpillow hyaloclastite	Spilite	–	14.0	0.2	–	14.2	–	2.55
SG14-9	431959	2741288	Interpillow hyaloclastite	Spilite	–	7.7	19.6	–	27.3	–	2.58
RWO1-ST46-a	433738	2716376	Interpillow hyaloclastite	Spilite	–	14.9	0.4	–	15.5	–	2.37
RWO1-ST46-b	433738	2716376	Interpillow hyaloclastite	Spilite	–	13.8	0.4	–	14.2	–	2.51

[a]Available only for a subset of the listed spilites and epidosites. Spilite: pervasive albite + chlorite + titanite + Fe-oxide ± quartz ± actinolite ± relict augite ± epidote; Epidosite: pervasive epidote + quartz + titanite + Fe-oxide ± relict chlorite ± relict augite. [b]Normalized to exclude volume fractions of calcite, hematite, titanite, titanomagnetite, and pore space: 0 vol.% = endmember spilite, 100 vol.% = endmember epidosite. [c]No correction applied for calcite clogging of pores or for presence of empty microfractures. [d]Calculated from carbon concentration determined by CNS analysis (see text). [e]Qualitative abundance based on SEM observations of thin sections: 2.0 = common; 0.5 = rare. [f]Corrected porosity = measured porosity + vol. frac. calcite − vol. frac. microfractures. See text for details. [g]Corrected for Klinkenberg effect but not corrected for late calcite clogging or for empty microfractures (see text).

The results were corrected for the Klinkenberg effect. As sub-seafloor in situ pressures are known to affect permeability (Christensen & Ramananantoandro, 1988; Gilbert & Bona, 2016; Karato, 1983), all measurements were performed at 50 MPa effective pressure, corresponding to the mean estimate for the Semail upper crust during spilite and epidosite alteration (Section 6.2). Measurement uncertainties are <10%.

As described in Section 4.2, our samples are essentially free of open microfractures induced by outcrop weathering. However, for a few of the samples, the above measurements underestimate the rock-matrix permeability at the time of spilite and epidosite alteration owing to the presence of later pore fillings of calcite, which presumably block otherwise permeable pathways through the rock matrix. After first measuring the permeability of test samples we removed their calcite by leaching in acetic acid and then remeasured their permeability. Unfortunately, this also unclogged calcite-generation microfractures and led to unrealistically high permeabilities, and so we abandoned this approach. The samples that contain calcite are therefore identified in our results and their reported permeabilities are treated as minimum values.

4.4. Simulations of Hyaloclastite Permeability

Fluid flux through a geometrically simplified 2D pillow stack was simulated numerically to constrain the permeability of fragile interpillow hyaloclastites that were not amenable to laboratory measurements. The model setup is based on the field observations of progressive epidotization of interpillow hyaloclastites, pillow cores and rims summarized in Section 2.2, on the tubular shape of individual pillows, and on the geometry of the pillow stacks akin to tight bundles of interconnected tree roots (Figures 2a and 2b). The setup consists of three stacks of four pillow tubes, offset vertically by half the tube height and connected via interpillow matrix (Figure 2c). The bounding tubes are 1 m and the central pillows 2 m long, each 48 cm high. Each tube consists of a core enveloped by symmetrical rims, which are both assigned the average isotropic permeabilities measured in this study. The geometric model was discretized into a fine mesh and Darcy flow was simulated using the software PFLOTRAN (Lichtner, 2007). Estimates of the water–rock ratios required to generate incipient, intermediate and complete epidosite alteration stages via the spilite-to-epidosite reaction were adopted from the detailed reactive transport simulations of Weber et al. (2021). With the permeability of the hyaloclastite as the only remaining unknown, the possible range of its permeability was then found by trial and error, such that the required water–rock ratios could be reproduced. This approach yields an isotropic permeability of the hyaloclastites at the cm^3 scale, compatible in scale with the laboratory measurements of pillow cores and rims.

4.5. Estimating Volume Fractions of Textural Zones in Pillow Stacks

To enable upscaled estimates of permeability for entire pillow stacks, the volume fractions of their component textural zones (pillow cores, pillow rims and interpillow hyaloclastites) were estimated. Digital field images of pillow stacks oriented perpendicular to the lava extrusion direction (Figure 3) were used to determine the areal proportions of the textural zones using the software *Fiji/ImageJ*. Although spilitized pillow cores and rims have different permeabilities (see below), the textural boundary between them is not visible at the scale of the outcrop images. Therefore, to find the average fractions of rim and core zones, we analyzed an image of a pillow stack that shows light green epidosite alteration exclusively in the pillow cores (Figure 3a). Field and petrographic observations in Gilgen et al. (2016) and in the present study show that such *intermediate epidosite* outcrops reliably distinguish pillow cores from pillow rims. The image was digitized into separate layers of polygons for the cores and for the entire pillows (core + rim). The separate layers were then converted into binary colored images (Figures 3c and 3d) and processed to find their respective areas. As the pillows can be approximated as cylinders (Figure 3b), we assume that the measured area fractions of pillow core, rim and hyaloclastite are equal to their volume fractions. We also assume that these proportions apply equally to both spilite and epidosite lava stacks, because the spilite-to-epidosite reaction does not change pillow dimensions, only their porosity (Weber et al., 2021).

5. Results

5.1. Compositions, Petrography, and Pore Types of Altered Lavas

Major-element compositions of the investigated samples are provided in Table S3 of Supporting Information S1.
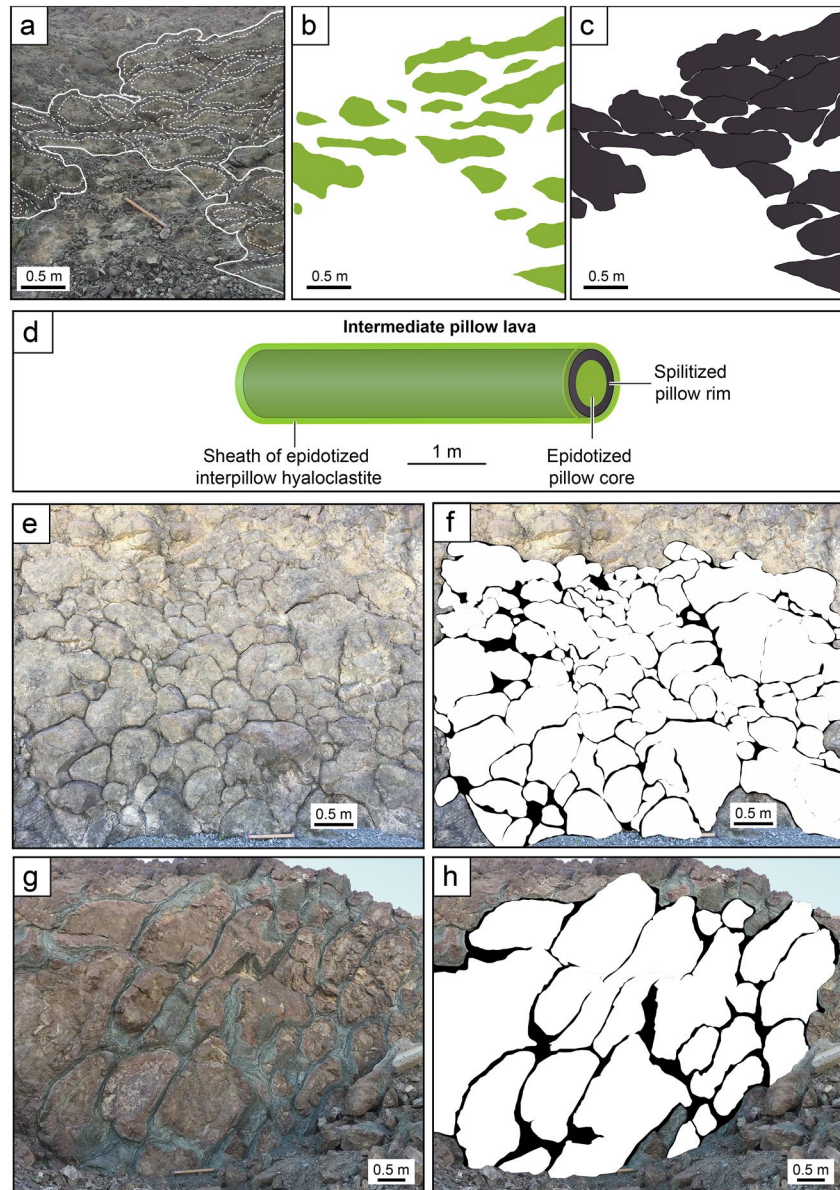
Figure 3. Outcrop photographs and tracings of Geotimes pillow lavas used to upscale drill plug analyses of rock-matrix porosity and permeability to outcrop scale. The images are oriented perpendicular to the average pillow extrusion direction. Younging direction is toward top left. (a) Intermediate-stage epidosite pillow outcrop, with epidotized pillow cores and spilitized pillow rims. (b) Polygons of pillow core areas from (a). (c) Polygons of pillow area (core + rim) from (a). (d) Schematic 3D diagram of intermediate-type pillow tube. (e) Spilite outcrop with relatively thin interpillow hyaloclastites. (f) Outcrop (e) with traced black interpillow hyaloclastites and white pillow interiors (core + rim). (f) Outcrop of large spilitized pillows with relatively thick interpillow hyaloclastites. (h) Outcrop (f) with traced black interpillow and white pillow interiors.

5.1.1. Spilitized Pillow Basalts

All the spilite samples are glass-free and consist of 80–100 vol.% hydrothermal minerals. Many of the samples have endmember spilite mineralogy and some contain slightly elevated amounts of epidote and quartz. Their porosities are strongly influenced by the igneous textures inherited from their MORB-like basalt to basaltic-andesite precursors. Thin-section petrography of the ghost igneous textures and examination of immobile trace-element ratios distinguished two types of pillow lavas. Type 1 ("evolved") pillows (Figures 4a and 4b) are most common and have the following features relative to Type 2: (a) more abundant vesicles; (b) higher former glass abundance (now entirely altered to chlorite intergrown with other fine-grained hydrothermal minerals); (c) plagioclase
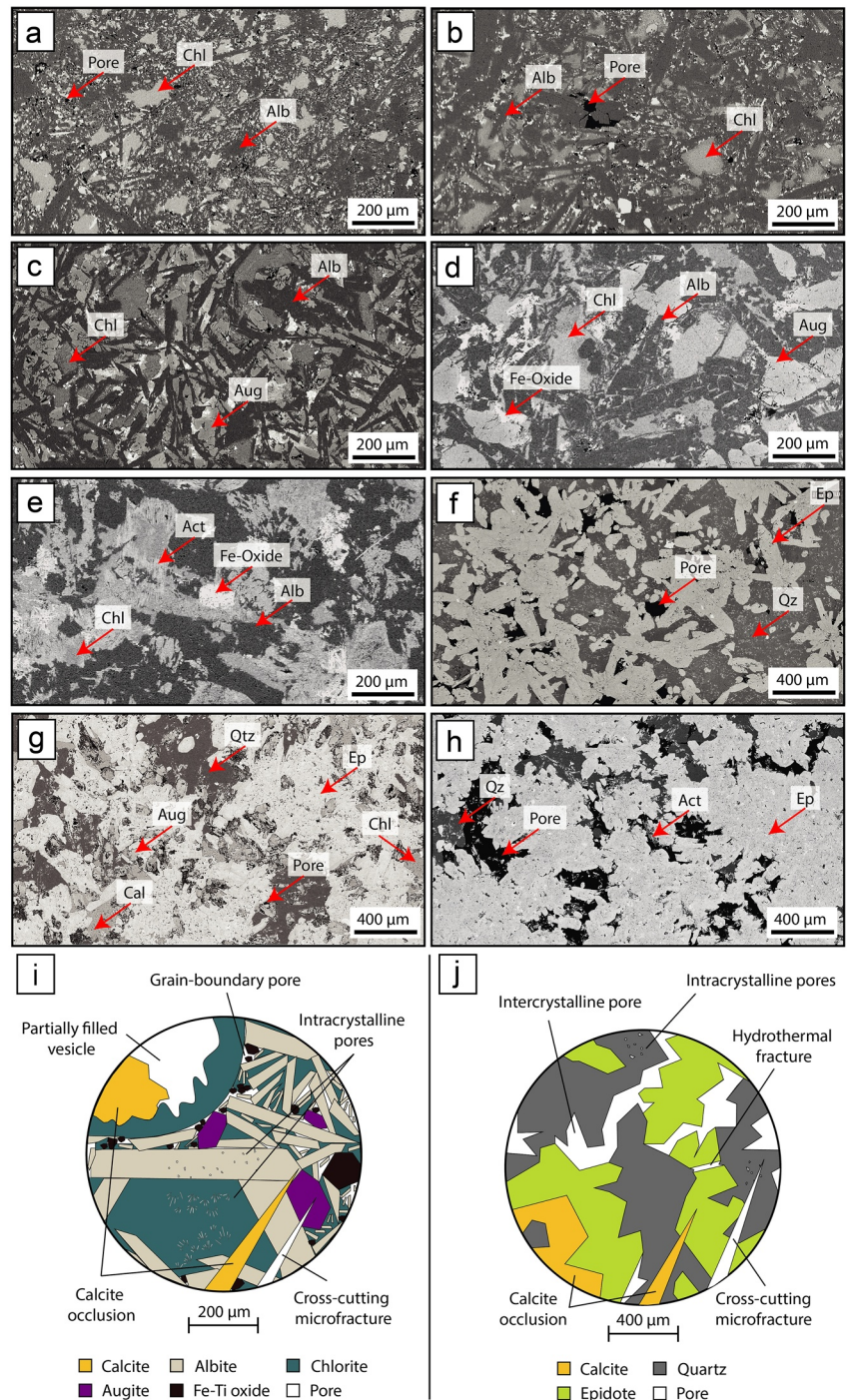
Figure 4. SEM–BSE microphotographs and diagrams of spilite and epidosite alteration textures in Geotimes lavas and SDC dikes, illustrating pore types including late obduction and weathering features. Note different scales between subfigures. (a) Spilite alteration in rim of evolved pillow lava, with intercrystalline pores. (b) Spilite alteration in core of evolved pillow lava, with intercrystalline pores. (c) Spilite alteration of primitive pillow lava core. (d) Spilite alteration of massive sheet flow. (e) Spilite alteration of dike. (f) End-member epidosite alteration with large intercrystalline pores. (g) Partial epidosite alteration containing relict igneous augite and spilite-generation chlorite. (h) Partial epidosite alteration of dike showing relict spilite-generation actinolite and large intercrystalline pores. (i) Pore types and late calcite in spilites. Intercrystalline pores at grain boundaries exaggerated compared to panels (a–e). (j) Pore types and late calcite in epidosites.

microphenocrysts (now completely metasomatized pseudomorphically to albite) that crystallized after the rare augite microphenocrysts; (d) elevated concentrations of immobile Zr (>90 µg/g) and Y (>30 µg/g) (Figure S1 in Supporting Information S1; values "this study" in Table S1 of Supporting Information S1) indicating evolved degrees of igneous fractionation, all presumably due to higher initial H_2O content (Feig et al., 2006). The vesicles in this pillow type are now empty or partly to completely filled by chlorite, and the groundmass is composed of fine-grained, pseudomorphic albite laths, occasionally small relict augites and interstitial chlorite (Figures 4a and 4b).

Type 2 ("primitive") pillows (Figure 4c) are less common; they contain rare vesicles and initially had less glass (now entirely altered to chlorite) and they have lower concentrations of Zr (<90 µg/g) and Y (<30 µg/g; Figure S1 in Supporting Information S1; values "this study" in Table S1 of Supporting Information S1) indicating less evolved fractionation and presumably lower initial H_2O content. They are also coarser-grained and have an ophitic texture of late augite microphenocrysts enclosing early plagioclase laths (now entirely metasomatized pseudomorphically to albite), with minor interstitial chlorite (Figure 4c). The volumetric ratio of relict augite to albite in evolved pillows varies from 0:20 to 1:20, whereas in primitive pillows the ratio is closer at 1:3 to 1:2. In both pillow types, the rims (outer 5–20 cm of the pillows; Figure 4a) are composed of finer relict igneous and hydrothermal crystals than the pillow cores (Figure 4b).

The vesicles in the pillows vary from 50 µm to 2 mm diameter, but they are not generally abundant. Thus, micropores at crystal boundaries and between plates and fans of chlorite are the dominant pore types (typically <20 µm diameter; Figures 4a–4c). In both magmatically evolved and primitive spilites, the 3D pore distribution is essentially isotropic, with only occasional elongation of vesicles due to continued lava movement after gas exsolution.

Spilites with 10–30 vol.% epidote + quartz often show additional pores where albite is replaced by epidote. These features can only be distinguished in thin section and otherwise the hand samples have the appearance of end-member spilites.

5.1.2. Dikes and Massive Sheet Flows

Spilitized dikes and sheet flows display larger crystal sizes than pillows and are not easily distinguished as primitive or evolved in thin section. They both contain large (∼200 µm) augite and albitized plagioclase crystals, and generally only minor chlorite is present due to the lack of precursor volcanic glass (Figures 4d and 4e). In some dikes actinolite replaces augite. Although Zr and Y contents vary somewhat, they do not seem to correlate with texture or pore types. The main pores are at grain boundaries, similar to those in Figure 4i. Amygdules are rare. Sizes of micropores vary between dikes and massive sheet flows but are usually <50 µm diameter and less abundant than in pillow lavas.

5.1.3. Epidosites

Epidosites with endmember mineralogy (∼90–100 vol.% epidote + quartz) have isotropic, coarsely crystalline textures that appear essentially identical whether in pillows lavas, massive sheet flows or dikes. They are composed of intergrowths of euhedral quartz and epidote arranged in idioblastic to granoblastic textures (Figures 4f and 4h; see also Gilgen et al., 2016; Weber et al., 2021). Inherited igneous textures are manifested by the slight decrease in crystal sizes from pillow cores to pillow rims, by the presence of vesicles (either open or more commonly filled by epidote fans and euhedral quartz) in epidotized lavas, and by the ghost groundmass texture revealed by titanite crystallites within epidote and quartz, which trace the outlines of former albite laths. Epidote and quartz are free of these titanite inclusions only where they replace former albite or fill vesicles. Inclusions of earthy hematite and relict igneous titanomagnetite are present in epidote in some samples but are limited to a few vol.% of the rocks. Most epidosites contain ∼30–90 vol.% epidote + quartz with finer crystal sizes, rare idioblastic textures, and they commonly retain chlorite, augite and actinolite inherited from the spilite precursors (Figure 4g).

Large intercrystalline pores (50–200 µm diameter; Figures 4f and 4h) are abundant in endmember epidosites. In near-endmember epidosites, pores are particularly noticeable around augite and actinolite (Figure 4g). In non-endmember epidosites, dissolution of some of the spilite-stage albite and chlorite has enlarged pores along crystal boundaries. Other minor pore types are hydrothermal fractures in epidote and quartz grains that have been partly or completely filled by further epidote and quartz precipitation, and pores in epidote fans that fill former vesicles (Figure 4j). Typical post-epidosite macro- and microfractures and clogging of pores by late calcite are shown in Figure 4j. In our fracture-free epidosite samples, the 3D distribution of matrix pores is isotropic.
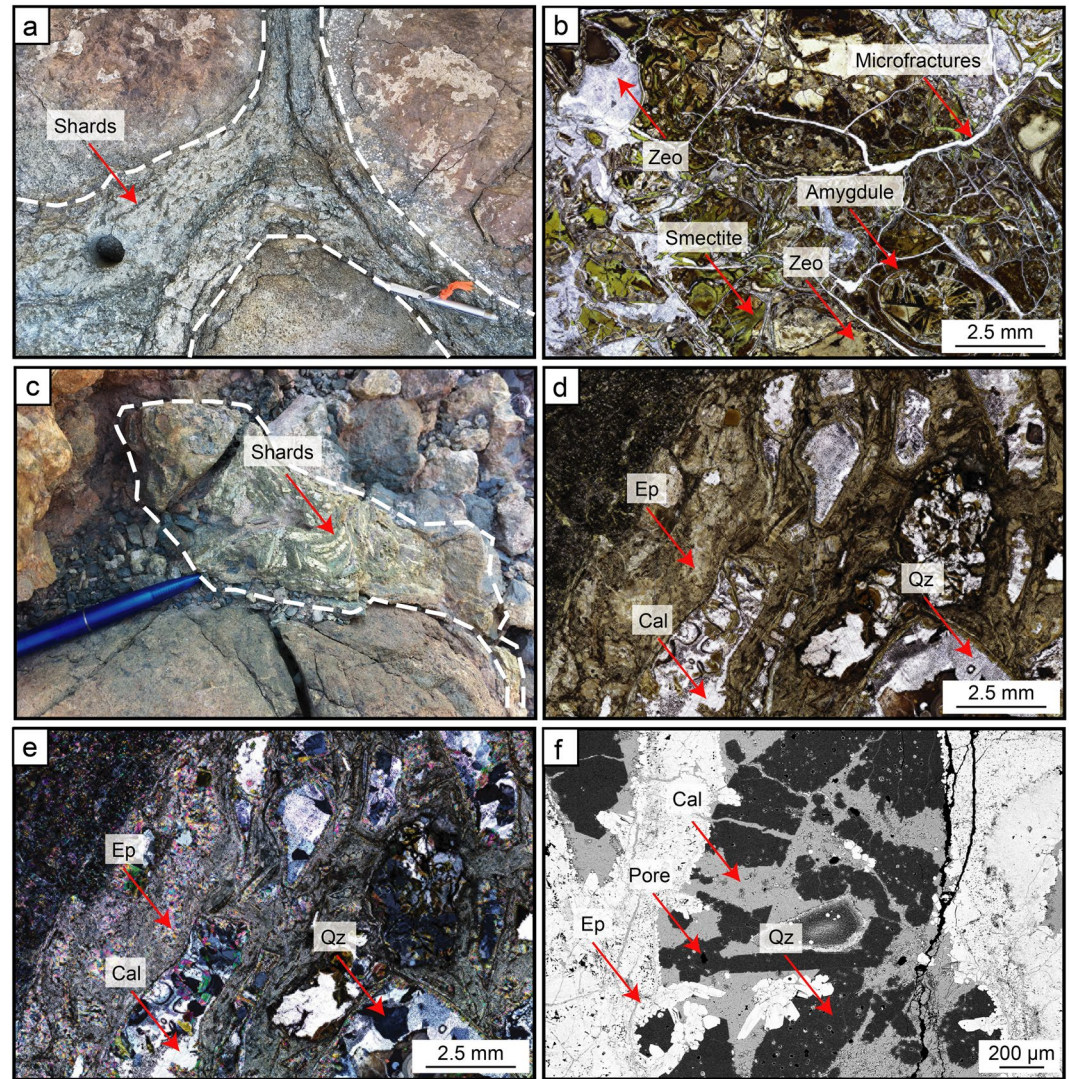
Figure 5. Textures of interpillow hyaloclastites at pillow triple junctions. (a) Outcrop of spilitized interpillow hyaloclastite (outlined) showing dark chlorite pseudomorphs of former glass shards altered to chlorite. Drill hole of a plug sample is visible. (b) Microphotograph in plane-polarized light (PPL). Spilitized hyaloclastite with abundant smectite and zeolite, as well as microfractures potentially caused by outcrop weathering. (c) Outcrop of epidosite alteration of interpillow hyaloclastite (outlined) showing pale pseudomorphs of former glass shards. (d) Microphotograph (PPL) of epidosite alteration of hyaloclastite. Green epidote matrix surrounding quartz–calcite pseudomorphs of former glass shards. (e) Same view as (d) in cross-polarized light. (f) Close-up SEM-BSE image of a pale shard pseudomorph in (c), showing epidosite-stage quartz replaced by late calcite.

5.1.4. Hyaloclastites

Hyaloclastites in spilitized interpillow zones display chlorite-green color in outcrop. They consist of platy and angular chloritized pseudomorphs of former glass shards occasionally containing amygdules of chlorite ± zeolite ± quartz (Figure 5a). At the outcrop scale two main textures are observed. In the wide triple junctions between pillows, former glass shards are large (up to 2 cm diameter) and randomly oriented. Pores up to several millimeters in diameter are common. In contrast, the envelope of hyaloclastite around the remainder of the pillows is finer grained and devoid of macroscopic pores. The former shards in these envelopes are aligned parallel to the pillow rims, imparting a preferred planar orientation to the hyaloclastite. Micropores are common around chlorite. Hand samples and thin sections of hyaloclastite contain many open microfractures and although some of these were likely open during hydrothermal circulation, they cannot be distinguished from late weathering fractures. Thin sections of spilitized hyaloclastite show a high abundance of smectite and zeolite (Figure 5b).

Rare, larger accumulations of massive hyaloclastite (0.3–3 m thick zones) in the pillow stacks consist of fine, vesicular fragments but lack the large platy shards observed in interpillow zones (Figure 5a).

Formerly spilitized hyaloclastites that have been replaced by epidosite (Figure 5c) have high tenacity, in contrast to their fragile, chloritized precursors. The pale shards in Figure 5c are strikingly similar in texture to the chloritized shards in Figure 5a; they may consist of quartz, epidote + quartz, or epidote + chalcedony, often with late pore fillings of calcite (Figures 5d–5f). The fine-grained matrix surrounding the shards is replaced by epidote $\pm$ quartz (Figure 5e). Pores are situated between euhedral quartz and epidote (although not as clearly as in the pillow-matrix replacement in Figure 4) and they are often filled by late calcite. As in the spilitized hyaloclastites, open or calcite-filled microfractures are present (Figure 5f), mostly cross-cutting and hence postdating the epidotization. However, some of the microfractures appear to be coeval with the epidosite alteration.

5.2. Quantitative Rock-Matrix Porosity and Permeability

Results of our measurements of rock-matrix porosity and permeability are shown in Figure 6, categorized by hydrothermal alteration type and igneous rock morphology (pillow cores, pillow rims, interpillow hyaloclastites, massive sheet flows, and dikes).

5.2.1. Rock-Matrix Porosity

Spilitized endmember dikes and dikes with <30 vol.% epidote + quartz have relatively low porosities ($\phi \leq 5$ vol.%), whereas massive flows and pillows both have higher ϕ of 4.5–12 vol.% (Figure 6a). Within individual spilitized pillows, rims are less porous than cores. Evolved pillows have higher average porosities than primitive pillows, consistent with their differences in vesicularity. The highest porosities among spilites are in interpillow hyaloclastites, with ϕ of 14–27 vol.%.

Epidotized interpillow hyaloclastites have porosities similar to or lower than their spilitized precursors (Figure 6a). All other types of epidosites have porosities up to two times higher than their spilite equivalents. The ranges of values from epidotized dikes, massive sheet flows and primitive pillow cores overlap and their averages are also similar at ~14 vol.%. Evolved pillow rims and pillow cores have slightly higher averages, again presumably reflecting their inheritance of more vesicles compared to dikes.

5.2.2. Rock-Matrix Permeability

Regarding the permeability of the spilitized hyaloclastites, our hydraulic simulations of the schematic pillow stack in Figure 2a take advantage of the field and petrographic findings that epidosite alteration occurs after spilite alteration, and that interpillow hyaloclastites are epidotized before pillow cores and pillow rims (Section 2.2). The simulations show that this sequence of alteration will occur only if the spilite interpillows have permeabilities between 10^{-17} and 10^{-15} m^2 (plotted in Figure 6b). If the hyaloclastites had permeabilities below 10^{-17} m^2, then pillow cores would become epidotized before the hyaloclastites, contrary to the observed alteration patterns. If the hyaloclastites had permeabilities higher than 10^{-15} m^2, then flow and epidotization would occur exclusively in the hyaloclastites, whereas pillow interiors would never be epidotized, contrary to the observations. Simulations were repeated throughout the range of measured permeabilities in pillow cores. These iterations confirmed that, for our simplified model geometry, the ratio of volumetric fluxes through the core and interpillow regions during epidotization is essentially a function of their permeability ratio.

For all igneous rock morphologies and for both spilite and epidosite alteration types, permeability trends mimic porosity trends (Figure 6b). Within each pillow lava the rim is less permeable than the core and evolved pillows are more permeable than primitive pillows. Dikes and massive sheet flows have permeabilities at the lower range of values for pillows. These results are compatible with the expected relative order of spilite permeabilities deduced from field criteria, as defined in Equation 1.

Permeabilities of epidosites have a larger range than those of spilites. The highest permeabilities (~3.5×10^{-16} to 3×10^{-15} m^2) are in endmember epidosites free of any calcite clogging. Values for samples containing 4–10 vol.% calcite (represented by orange rings in Figure 6b) represent minimum permeabilities for the spilites and epidosites.

5.2.3. Porosity-Permeability Relationships

The relationship between porosities and permeabilities of the samples with no or only minor calcite clogging is shown in Figure 7. The porosity–permeability trend of spilites shows a positive correlation, but several samples
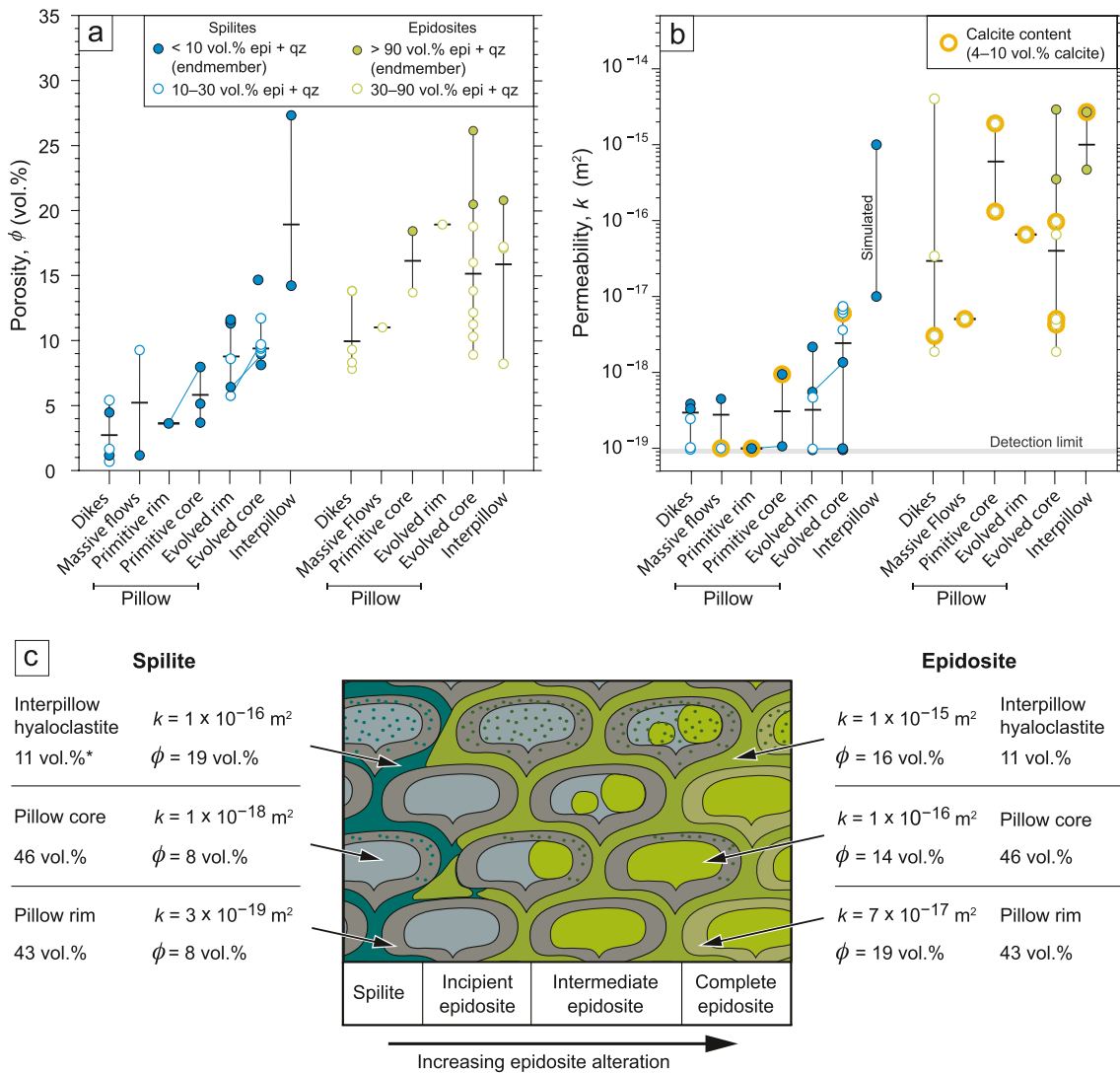
Figure 6. Results of rock-matrix porosity and permeability (this study) categorized by igneous rock morphology, extent of magmatic fractionation (primitive vs. evolved) and hydrothermal alteration type. All values are from measurements of drilled plugs, except for simulated permeabilities of spilite interpillow hyaloclastite (see text). (a) Rock-matrix porosities, corrected for clogging by late calcite. Horizontal bars denote averages of indicated ranges. Diagonal tie-lines join rim–core pairs from individual pillows. (b) Rock-matrix permeabilities (sample set differs slightly from (a). All values provided in Table 1). Horizontal bars denote geometric means of indicated ranges. No calcite-clogging correction could be made, therefore samples containing calcite are marked by orange rings. Diagonal tie-lines join rim–core pairs from individual pillows. (c) Schematic diagram of progressive epidosite alteration of pillow outcrops with field-scale zones identified by Gilgen et al. (2016), summarizing average porosities and geometric means of permeabilities from (b) and (a) for pillow cores, pillow rims and interpillow hyaloclastites (combined primitive and evolved data). Plausible maximum values are discussed in Section 6.5. Note: vol.%* = mean volume fraction of rock type relative to total outcrop volume, k = permeability (m²), ϕ = porosity (vol.%). Full list of sample porosities and permeabilities provided in Table 1.

lie on the detection limit of our permeability measurements, precluding fitting of a meaningful trend line to our data set. Pristine (calcite free) epidosites also follow a positive porosity–permeability trend, broadly represented by the following exponential fit (line 2 in Figure 7; $R^2 = 0.21$):

$$k_{\text{epidosite}} = 5.1 \times 10^{-19} e^{0.4881\phi} \tag{3}$$

where k is permeability (m²) and ϕ is porosity (vol.%).

No systematic difference in the porosity–permeability relationship is observed between different volcanic rock morphologies. However, pillows and epidotized interpillow hyaloclastites are generally shifted to higher permeabilities than dikes, as already shown in Figure 6. Spilites clogged by minor late calcite are not displayed in Figure 7 but they generally overlap with the pristine spilites (see Table 1 for values). In contrast, clogged epidosites are
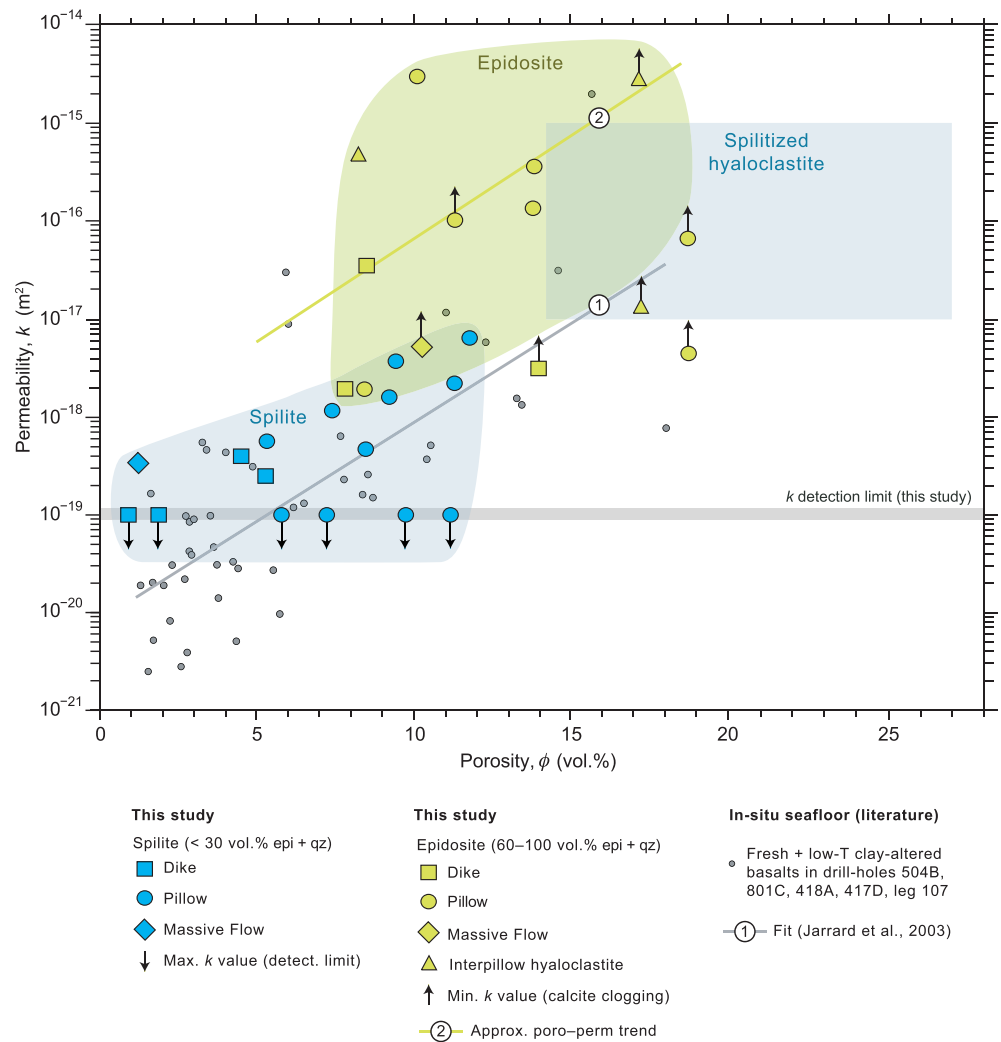
Figure 7. Relationship between rock-matrix porosity and permeability in spilite and epidosite samples from this study, compared to fresh and low temperature clay-altered basalts recovered from drill holes in in situ basaltic seafloor (Jarrard et al., 2003 and references therein). "Spilitized hyaloclastite" field based on measured porosity range and simulated permeability (see text). "Spilite" and "Epidosite" fields encompass measured data. Measured porosity values from this study are corrected for late calcite clogging, but measured permeability values are uncorrected (clogged samples denoted by upward arrowheads pointing toward true values). Line 1: fit to data in Jarrard et al. (2003), adopted to describe porosity–permeability trend of our measured spilites. Line 2: porosity–permeability trend fitted to calcite-free (unclogged) epidosites.

included and lie to the right of the pristine epidosite field, owing to their high calcite-corrected porosities but moderate permeabilities uncorrected for calcite clogging. Samples with notable open microfractures are excluded because their permeability values cannot be corrected (see Table 1 for values).

5.3. Volume Fractions of Textural Zones and Bulk Porosity of Pillow Stacks

Image analysis of the pillow stack altered to intermediate epidosite (Section 4.5 and Figure 3a) shows that cores make up ~52 vol.% and rims ~48 vol.% of each pillow on average. Analyses of 15 images from six outcrops (Figures S2–S4 in Supporting Information S1) demonstrate a large range of volume fractions for hyaloclastites of ~2–26 vol.% (Table S2 in Supporting Information S1), with an average of ~11 vol.%. Thus, expressed as fractions of an average pillow stack, pillow cores make up ~46 vol.%, pillow rims ~43 vol.% and interpillow hyaloclastite ~11 vol.%.

Weighting the average porosity and permeability measurements of the three textural zones in pillows (Figure 6c) by the above volume fractions yields upscaled bulk rock-matrix porosities (ϕ) for entire pillow stacks. Thus,

spilitized lava stacks at the 10^4 m^3 scale are calculated to have $\phi_{\text{spilite}} \approx 9$ vol.% whereas epidotized stacks have $\phi_{\text{epidosite}} \approx 16$ vol.%. Estimates of bulk permeability of pillow stacks are addressed below in Section 6.4.

6. Discussion

6.1. Reliability of Results

Only a limited set of 40 samples could be analyzed for porosity and permeability in our study (Figure 6), and a further six samples were analyzed for porosity only (Table 1). This reflects our stringent sample selection criteria, designed to avoid the ubiquitous weathering fractures in the Oman outcrops and to minimize the presence of late calcite. Nevertheless, based on our extensive field experience in the Semail ophiolite, we are confident that these samples are typical of the alteration types and of the variety of rock types in the axial Geotimes lavas and comagmatic SDC.

Six of the analyzed samples contain rare or numerous open microfractures of post-hydrothermal origin, but their contributions to the sample porosity could be corrected using fracture volumes estimated from SEM-BSE images. Also the pore space filled by late calcite could be added to the measured porosity based on bulk calcite analyses of the samples performed after the porosity and permeability measurements. Unfortunately, such corrections could not be applied to the permeability results of the affected samples. Therefore, our reported permeabilities are likely to be slightly underestimated owing to pore clogging by minor calcite.

It remains possible that our small sample set does not capture the full range of rock-matrix porosity and permeability in the investigated rock units. However, the systematic differences in hydraulic properties between the various rock morphologies (Figure 6) clearly correlate with the intensities of alteration visible in the field (Equation 1) and hence with the associated variation in water–rock ratios (Weber et al., 2021), consistent with our results.

6.2. Porosities and Permeabilities Representative of In Situ Hydrothermal Conditions

As our porosity measurements were conducted at room P–T, the question arises as to whether the values are valid for the original in situ P–T conditions of active spilite and epidosite alteration at depth in the Semail crust. Stratigraphic reconstructions to the base of the SDC (Belgrano et al., 2019, 2021) and fluid inclusion data (Richter & Diamond, 2022) suggest that the studied alteration occurred at temperatures of 200–440°C and that maximum and minimum pressures through to the base of the SDC varied as follows: $P_{\text{confining}} = P_{\text{ocean}} + P_{\text{lithostatic}} = 4$ 4–190 MPa and $P_{\text{effective}} = P_{\text{confining}} - P_{\text{hydrostatic}} = 8$–90 MPa (mean $\approx$ 50 MPa). As epidosite alteration mostly occurred during post-axial Tholeiitic Alley time (Section 2.2), the maxima of these pressure ranges include the Tholeiitic Alley overburden above the axial SDC and Geotimes lavas. Calculations using the thermoelastic properties of the spilite and epidosite mineral assemblages show that the porosity of both alteration types increases by at most 2.4 vol.% during heating and compression to the original in situ conditions (Brett-Adams et al., 2021). Compared to the measured variation in porosity between our samples, this change is negligible.

To allow for the effect of in situ pressure on permeability, our measurements were made at an effective pressure of 50 MPa, equal to the mean $P_{\text{effective}}$ estimated above for the Semail upper crust during spilite and epidosite alteration. To determine the effect of heating to in situ temperatures, Brett-Adams et al. (2021) carried out permeability measurements on some of the same samples as this study at $P_{\text{effective}} = 50$ MPa and at temperatures up to 450°C. The temperature change decreased permeability by 45%–80%, regardless of the alteration and rock type (whether spilitized or epidotized pillows or dikes). However, this decrease is insignificant compared to the three orders of magnitude inter-sample variation shown in our room-temperature permeability measurements (Figure 6b), and so it can be ignored. We conclude that the porosities and permeabilities reported in Table 1 and in Figures 6 and 7 can be taken as closely representative of the values at the original in situ hydrothermal P–T conditions of spilite and epidosite alteration in the Semail ophiolite.

6.3. Porosity-Permeability Correlations

The positive correlation between the porosity and permeability of our spilites at the analyzed drill-plug scale (Figure 7) is similar to that of fresh and low-T clay-altered basalts in drill core extracted from in situ seafloor

(gray dots in Figure 7), as summarized by Jarrard et al. (2003; and references therein). The trend of these scattered literature data is approximated by the following exponential fit (line 1 in Figure 7; $R^2 = 0.46$):

$$k = 8.28 \times 10^{-21} e^{0.463\phi} \tag{4}$$

where k is permeability (m^2) and ϕ is porosity (vol.%). Our spilites that plot on the detection limit for this study (indicated by downward arrows in Figure 7) presumably have the same ultralow permeabilities as many of the samples from the in situ seafloor. Thus, our spilite data appear to overlap well with the literature data, which suggests that Equation 4 can also be used to describe the mean hydraulic properties of our spilites.

Epidosites generally have much higher rock-matrix permeabilities than spilites for porosities between ∼7 and 12 vol.% (Figure 7). This may reflect the interconnectedness of the large pores in the relatively coarse-grained granoblastic epidosites compared to the fine-grained, tortuous texture of the spilites. The porosities of the epidosites that plot to the right of the pristine samples in Figure 7 are corrected for calcite clogging, but their permeabilities are not corrected (indicated by upward arrows). Since the late-stage hydrothermal fluid that precipitated calcite (Richter & Diamond, 2022) would have preferentially infiltrated the most permeable of the epidosites, it can be assumed that the clogged samples had pre-calcite permeabilities much higher than their measured values. Thus, the data array in Figure 7 suggests that epidosites with porosities of 15–18 vol.% could in general have permeabilities of 1×10^{-14} or more.

6.4. Distribution of Porosity and Permeability in Pillow Lavas and Their Consequences for Progressive Epidosite Alteration

Our analyses of spilitized Geotimes pillow lavas have confirmed the strong zonation in permeability deduced in the field from the pattern of spilite replacement by epidosite (Equation 1 and Figure 6c; Gilgen et al., 2016). Thus, hyaloclastites are the first parts of the initially spilitized pillow stacks to be replaced by epidosite (creating *incipient epidosites*) because their permeability is 1–4 orders of magnitude higher than that of the pillows. Pillow cores are next epidotized (creating *intermediate epidosites* in which only pillow rims remain spilitized) because they are ∼0.5–1 orders of magnitude more permeable than spilitized pillow rims. Areas of such *intermediate epidosite* are widespread in the Geotimes pillows throughout the ophiolite, even though the outer surfaces of the pillow rims are in direct contact with the highly permeable hyaloclastite. Evidently, epidosite-forming fluids (which have a distinct chemistry to spilitizing fluids; Richter & Diamond, 2022; Weber et al., 2021) infiltrated the pillow cores from below the pillow stack, presumably via fractures or hyaloclastites, and then migrated upwards and laterally through the root-like network of upward-branching pillow cores. Finally, after prolonged fluid flux through this tortuous path (corresponding to high outcrop-scale water–rock ratios; Weber et al., 2021), the low permeability pillow rims were also epidotized, forming pillow stacks of *complete epidosite.*

6.5. Anisotropy and Upscaling of Permeability

To facilitate application of our results in large-scale thermal–hydraulic–chemical simulations, a first-order approximation of bulk permeability at the outcrop (10^4 m^3) scale can be derived by combining our laboratory measurements with constraints from field observations. In our opinion, this scale is sufficient for a representative elementary volume (REV), which captures the heterogeneities and anisotropy of the rocks that make up the volcanic crust and SDC.

The preceding discussion (Section 6.4) implies that hydrothermal flow through both the spilitized and epidotized pillow lavas in the Geotimes unit was highly anisotropic. As a simplified coordinate system to describe this anisotropy we denote the horizontal axis parallel to the long axes of the pillow tubes as x, the horizontal axis perpendicular to the tubes as y, and the vertical axis perpendicular to the tubes as z. The hyaloclastite enveloping the pillows is probably the least anisotropic of the component rock textures at the 10^4 m^3 scale, as its honeycomb-like distribution provides a connected 3D pathway for fluid flow in all directions. Within the pillow tubes, channeled flow parallel to x was clearly dominant versus flow across the tubes in the y and z directions, which was hindered by the low permeability of the pillow rims. Flow in the x direction entails simultaneous parallel flow through the three textural zones. Accordingly, upscaled bulk permeabilities for the pillow stack REV in the x direction are calculated by summing the permeabilities (k) of the hyaloclastite, pillow core and pillow rim, each weighted

by its mean volume fraction in outcrop. Using our maximum estimated permeability of spilitized hyaloclastite (Section 5.2.1) and mean pillow core and rim values in Figure 6c results in:

$$k_{x(\text{spilite pillow stack})} = 1.1(06) \times 10^{-16}\,\text{m}^2 \tag{5}$$

For comparison, using our mean permeability of spilitized hyaloclastite yields $k_{x(\text{spilite})} = 1.2 \times 10^{-17}$ m^2, demonstrating the sensitivity of these calculations to this part of the pillow stack. Using the predicted maximum epidosite value for hyaloclastites and pillow cores ($\sim 10^{-14}$ m^2) of from trend line 2 in Figure 7 and the average pillow rim value in Figure 6c, results in an upscaled value for *complete* epidosite of:

$$k_{x(\text{epidosite pillow stack})} = 5.7 \times 10^{-15}\,\text{m}^2 \tag{6}$$

In comparison, using all three mean epidosite values in Figure 6c, which are uncorrected for calcite clogging and include non-endmember epidosites, produce a lower permeability of $k_{x(\text{epidosite})} = 1.9 \times 10^{-16}$ m^2. Flow through the pillow stack in the y and z directions entails sequential flow across the pillow cores and rims, as well as simultaneous flow through the 3D hyaloclastite network. Permeabilities in these directions are therefore obtained by summing the hyaloclastite permeability and the harmonic mean of the pillow core and pillow rim permeabilities (same values as used for Equations 5 and 6), each weighted by their volume fractions:

$$k_y = k_{z(\text{spilite pillow stack})} = 1.1(04) \times 10^{-16}\,\text{m}^2 \tag{7}$$

$$k_y = k_{z(\text{epidosite pillow stack})} = 1.2 \times 10^{-15}\,\text{m}^2 \tag{8}$$

This calculation approach results in bulk permeabilities for the spilites that are essentially identical in all directions, as the contribution of the hyaloclastite vastly dominates the sum. A small difference is visible for the epidotized pillow stacks. These differences are negligible for all conceivable applications of these estimates.

Pillow lavas vastly dominate the axial Geotimes unit, although feeder dikes locally cross-cut the lavas. Massive lava flows appear only in the uppermost section of the unit. The upscaled rock-matrix porosities and permeabilities presented in this study for lava stacks can therefore be taken as representative of almost the entire volcaniclastic unit. Feeder dikes and massive flows have much lower permeabilities (Figure 6) and where present they tend to act as hydraulic barriers to fluid flow (as also noted for in situ oceanic crust, e.g., Bach et al., 2004). This behavior is evident at the field scale in the Geotimes lavas, where spilitized pillow stacks have been locally altered to complete epidosites, while the coeval feeder dikes and intercalated sheet flows show only minor epidosite alteration (Gilgen et al., 2016). The uniform rock-matrix textures of the Geotimes massive sheet flows suggest that they have approximately isotropic permeabilities. Thus, our few laboratory measurements can be used directly as permeability estimates at the 10^4 m^3 REV scale. Our two spilitized samples lie close to our experimental detection limit, with an average value of:

$$k_x = k_y = k_{z(\text{spilite massive flow})} = 2 \times 10^{-19}\,\text{m}^2 \tag{9}$$

Only one measurement is available for an epidotized massive flow, therefore the following can be taken as a first approximation:

$$k_x = k_y = k_{z(\text{epidosite massive flow})} \approx 1 \times 10^{-16}\,\text{m}^2 \tag{10}$$

Field observations show that individual dikes in both the SDC and the extrusive lavas have strong internal anisotropy with preferred flow parallel to the dike walls. For example, Figure 1f shows the common stripy appearance of epidosite alteration overprinting the core of a spilitized dike. Chilled margins make up about ~ 15 vol.% of the dikes, but we were unable to measure their permeability. Presumably it lies in the range of 1×10^{-20} m^2, below our detection limit. Permeability parallel to the spilitized dikes (in the xz plane) is thus given by the sum of this chilled-margin value and the average dike core value in Figure 6c, each weighted by its respective volume fraction:

$$k_{x(\text{spilite dike})} = k_{z(\text{spilite dike})} = 2.6 \times 10^{-19}\,\text{m}^2 \tag{11}$$

The permeability of the epidosite dikes in the xz plane is calculated similarly. The chilled margin and dike core are assigned the lower and upper values of the permeability range in Figure 6b, respectively:

$$k_{x(\text{epidosite dike})} = k_{z(\text{epidosite dike})} = 3.4 \times 10^{-15} \text{m}^2 \tag{12}$$

Permeability perpendicular to the spilite and epidosite dikes (y axis) is ~3 orders of magnitude lower, as given by the volume-weighted harmonic mean of the same values used for Equations 11 and 12:

$$k_{y(\text{spilite dike})} = 3.0 \times 10^{-21} \text{m}^2 \tag{13}$$

$$k_{y(\text{epidosite dike})} = 6.0 \times 10^{-18} \text{m}^2 \tag{14}$$

Equation 11 shows that the permeability of spilitized dikes is extremely low, even in the most favorable directions. This fits with the assumption that the in situ measured permeability of the SDC in young seafloor (e.g., 10^{-18} to 10^{-17} m^2 from Anderson et al. (1985) and Becker (1989)) is dominated by fractures. Nevertheless, the rock-matrix permeability of the Semail dikes was evidently sufficient to permit complete replacement of igneous plagioclase by hydrothermal albite, and to locally permit progressive epidotization of the spilitized rock matrix. In contrast, the permeability of completely epidotized dikes is ~4 orders of magnitude higher than that of spilites, and notably ~2–3 orders of magnitude higher than the fracture-dominated permeability of the SDC in in situ oceanic crust. A summary of the ranges calculated in this Section is shown in Figure 1b.

6.6. Implications for Porosity and Permeability of the Upper Oceanic Crust

6.6.1. Comparison of Spilites With Fresh and Low-Temperature Altered Basalts

Figure 8 compares our newly determined porosities and permeabilities of spilites with those of previously measured spilites, fresh oceanic basalts and oceanic basalts altered at low temperature to clay and zeolite assemblages. The literature data come from seven sites in in situ oceanic crust (five DSDP drill holes and two dredge sites) as well from the Semail and Troodos ophiolites.

In dikes and massive flows, our porosities and permeabilities are generally consistent with previous studies of spilites. The exception is permeability values of ~10^{-15} m^2 for dikes in hole 1256D (Gilbert & Bona, 2016); however, these values were measured using a Tiny-Perm II device, which in the same study on pillow lavas produced very high permeabilities compared to a standard permeameter (Gilbert & Bona, 2016). We do not consider this value to be accurate (see Filomena et al. (2014) for a detailed comparison of the techniques, cf., Gilbert & Bona, 2016) and so it is marked "x" for "dubious" in Figure 8. Despite the low temperature alteration of all the previously measured massive flow samples, their porosities are consistent with our spilitized massive flows. However, the one study of seafloor massive flows (Jarrard et al., 2003) shows up to two orders higher permeability than our samples. The one massive flow from the Troodos ophiolite with a higher porosity of ~17 vol.% is likely a vesicle-rich sample from an H$_2$O-enriched magma (Gillis & Sapp, 1997). The H$_2$O-poorer, MORB-like Geotimes massive flows that we have investigated are never vesicle-rich.

The larger range of porosities and permeabilities in pillow lavas compared to massive flows and dikes in the literature (Figure 8) also agrees with the variation we measured between individual pillow lavas. Those pillow lavas with the highest porosities and permeabilities in the literature have high vesicularity, for example, the Troodos basaltic-andesite samples have up to 20 vol.% vesicles (Gillis & Sapp, 1997) and the tholeiites from Hole 801C are also described as being vesicular (Jarrard et al., 2003). Extremely high permeability values from Hole 1256D were measured using the same Tiny-Perm II device as the high permeability dike mentioned above, including even gabbros with 10^{-15} m^2 (Gilbert & Bona, 2016), and so these values are likewise marked "x" for "dubious" in Figure 8. Otherwise, our measurements for spilitized Geotimes pillows overlap with the central range of porosities and permeabilities in the literature. This comparison shows that the vesicle-poor Semail Geotimes pillow have comparable hydraulic properties to MORB lavas. As ours is the first study to yield quantitative permeabilities for spilitized interpillow hyaloclastite, no literature comparison is possible. However, our findings that the hyaloclastite is by far the most permeable component of pillow stacks agrees qualitatively with previous work on fresh and low-T altered lavas (e.g., Coogan & Gillis, 2018; Seyfried et al., 1978).

Previous studies have reported that the porosity and permeability of fresh basalts is reduced by seafloor weathering, by shallow hydrothermal clay alteration (Gillis & Sapp, 1997; Johnson, 1980b), and by carbonate and
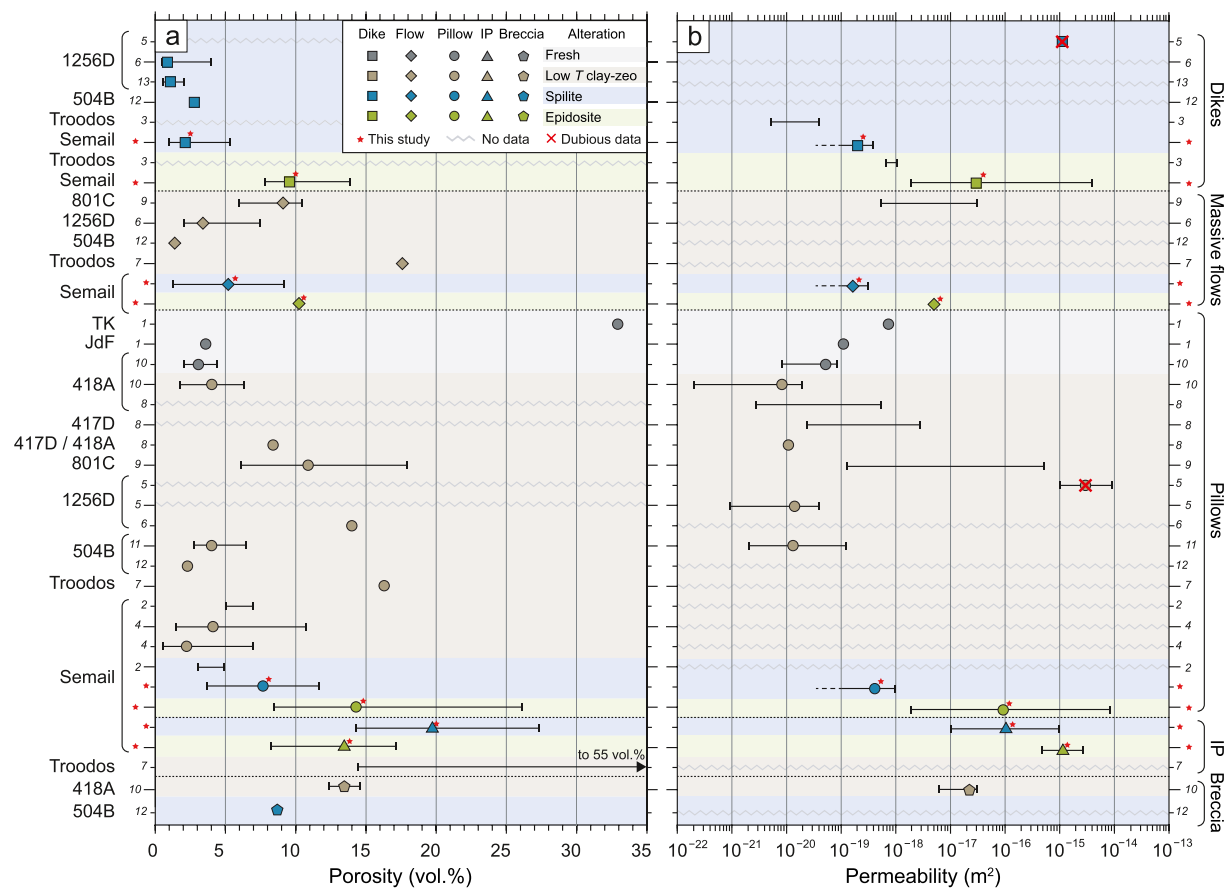
Figure 8. Comparison of matrix-porosity and matrix-permeability of basaltic rocks (shown from top to bottom: dikes, massive flows, pillow lavas, interpillow hyaloclastite = IP, breccias) in upper oceanic crust as a function of alteration type (different background colors: fresh basalt, low temperature clay-zeolite, spilite, epidosite) and locality. Data sources are indicated on the *y*-axes, with red asterisks denoting this study (pillow data combine cores and rims) and numbers denoting literature listed below. Range bars include averages (symbols) where available. Horizontal zigzag lines indicate that either no porosity or no permeability values are available for the specified samples. Samples marked x are dubious—see text for explanation. (a) Porosity. (b) Permeability, including the 1×10^{-19} m^2 limit of detection for our Semail data (dashed). [1]Christensen and Ramananantoandro (1988), [2]Christensen and Smewing (1981), [3]Coelho et al. (2015), [4]Einaudi et al. (2000), [5]Gilbert and Bona (2016), [6]Gilbert and Salisbury (2011), [7]Gillis and Sapp (1997), [8]Hamano (1980), [9]Jarrard et al. (2003), [10]Johnson (1980b), [11]Karato (1983), [12]Pezard (1990), [13]Violay et al. (2010).

zeolite precipitation in pores (Jarrard et al., 2003). It is thus surprising that there is little difference in porosity and permeability between the in situ seafloor samples and our Semail spilites. The overlap of the datasets in Figures 7 and 8 implies that thoroughly pervasive hydrothermal alteration at prehnite–pumpellyite to greenschist facies conditions does not markedly change the average hydraulic properties of the basalts. Section 5.1 and Figure 4 demonstrate that spilitization creates additional porosity where volcanic glass is replaced by chlorite, while vesicles become partially clogged by hydrothermal minerals. A possible explanation for the overlap of the datasets is that these two competing spilitization processes are approximately balanced, such that the bulk porosity and permeability remain similar to that of the igneous precursors. Owing to the ubiquitously intense alteration of the Geotimes lavas, no fresh samples are available to verify this explanation directly.

6.6.2. Epidosite Permeability

The spilite-to-epidosite reaction was previously predicted to increase porosity by 10–15 vol.%, based on estimates of the reaction stoichiometry and qualitative observations of the abundant porosity in thin-sections of epidosites (Cann et al., 2014; Harper et al., 1988). Reactive transport simulations predict similar increases of 8–11 vol.% depending on initial spilite mineralogy (Weber et al., 2021). Our results are the first quantitative measurements of porosity in epidosites, confirming that they are 9–14 vol.% more porous than their spilite precursors.

Our results also show that the jump in porosity during epidotization is associated with an increase in permeability by up to four orders of magnitude in endmember epidosites, reaching 4×10^{-15} m^2 (Figure 6b) or even

perhaps 10^{-14} m^2, as suggested in Section 6.3. The one previously published permeability measurement (Coelho et al., 2015) was performed on a partially epidotized sample from Troodos (i.e., it contains abundant relict chlorite from the spilite precursor), yielding $\sim 8 \times 10^{-18}$ m^2, similar to our measurements on some of our epidosites with lower contents of epidote + quartz.

6.6.3. Significance of Interpillow Hyaloclastites as Fluid Pathways

In the Troodos ophiolite, Gillis and Sapp (1997) estimated the macroscopic porosity in interpillow hyaloclastites (i.e., pore space visible in outcrop photographs, consisting of rock clast porosity + palagonite porosity of ~ 30 vol.% + porosity equivalent to calcite-filled zones), obtaining 25–55 vol.% in outcrops of fresh basaltic andesites and 14–28 vol.% in outcrops altered to low temperature clay assemblages. The latter values are essentially identical to the 14–27 vol.% found in our laboratory measurements of spilitized Geotimes interpillows (Figure 8a), underscoring the common high porosities of hyaloclastites.

In Figure 8 our Geotimes interpillow zones are clearly the most porous and permeable non-epidotized rocks in the altered upper crust, even higher than the breccias from DSDP Holes 418A and 504B. Moreover, interpillow hyaloclastites surround every pillow, constituting a connected network throughout the pillow stacks.

6.6.4. Application of Rock-Matrix Permeabilities to Simulate Hydrothermal Circulation in the Upper Oceanic Crust

The main application of measured permeabilities is in coupled numerical thermal–hydraulic and thermal–hydraulic–chemical simulations of fluid flow through the oceanic crust. However, rock-matrix permeabilities measured at the hand-specimen scale, as done in the present study, are currently not used in numerical simulations. In fact, there is a longstanding discrepancy of more than 3–4 orders of magnitude between hand-specimen permeabilities and the much higher crustal-scale values used by modelers (as recently highlighted by Gilbert & Bona, 2016). Most numerical models use crustal-scale permeabilities of $\sim 1 \times 10^{-16}$ to 4×10^{-11} m^2, which have been found by trial and error to reproduce known heat flow or fluid discharge fluxes (Fisher, 1998 and references therein; Hasenclever et al., 2014). Attempts have been made to measure crustal-scale permeabilities that corroborate these values, using a number of approaches. The highest values of 1×10^{-12} to 4×10^{-6} m^2 were found by treating fractures in the SDC with the parallel plate method, in which the 2D extent of the fractures is infinite (e.g., Semail ophiolite by Nehlig (1994); on-axis crust in the Troodos ophiolite by van Everdingen (1995); DSDP Hole 418A by Johnson (1980a)). However, this and other indirect methods, such as permeability calculated from heat flow, may be semi-quantitative and may overestimate permeability (Fisher, 1998). In contrast to fracture-based permeabilities, values measured in situ with drill-string packer tests yield a lower range of crustal scale permeabilities of 1×10^{-18} to 1×10^{-10} m^2 (e.g., Anderson et al., 1985; Becker, 1989; Becker & Davis, 2003; Becker & Fisher, 2000; Davis & Becker, 2002; Fisher, 1998). Nonetheless, this range of crustal-scale values is still orders of magnitude higher than the permeabilities of most hand specimens from ophiolites and in situ oceanic crust. Figure 8 shows that fresh basalts, most low temperature altered basalts, and spilitized dikes and pillows have permeabilities between 1×10^{-21} and 1×10^{-18} m^2.

Which component of permeability in the crust can reconcile the above discrepancies? Although parallel plate models for fracture permeability appear to produce erroneously high values, fracture permeability is a clear candidate to fill the permeability gap (e.g., Gilbert & Bona, 2016). Fractures have been documented in effusive lavas in ophiolites and drill holes (e.g., Christensen & Smewing, 1981; Gilbert & Bona, 2016; Gillis & Sapp, 1997; Johnson, 1980a) but they lack regionally representative quantification and realistic permeability estimates. On the other hand, as emphasized in Section 2.3, large tracts of the Semail Geotimes lavas are only sparsely fractured (Gilgen et al., 2016). As an alternative to fracture networks, the epidosites, breccias and hyaloclastites in Figure 8 are permeable enough to explain the lower values in the range of proposed crustal-scale permeabilities. Although epidosites undoubtedly constitute high permeability pathways, their role may only be relevant in some oceanic settings and so far they have been found very rarely in in situ oceanic crust (Gillis & Banerjee, 2000; Staudigel, 2014). In contrast, hyaloclastites and breccias are common and have the highest permeabilities of all upper crustal lava types. For example, breccias make up ~ 19 vol.% of the extrusive sequence in Hole 1256D (Tominaga et al., 2009), and hyaloclastites make up 7.5–18 area% of pillow outcrops mapped in Troodos (Gillis & Sapp, 1997) and 2–26 vol.% (average = 11 vol.%) of pillow outcrops in Semail Geotimes lavas (this study). Therefore, extensive and permeable hyaloclastite networks may be the dominant flow paths through pillow stacks in the large blocks of relatively unfractured lavas that are situated between major seafloor faults.

Our calculated bulk rock-matrix permeability of an average spilitized pillow stack, which takes into account hyaloclastite permeability, is the first estimate based on upscaling of hand-specimen measurements. The upper value of 1×10^{-16} m^2 overlaps with minimum values measured by packer tests in in situ crust and is 2–3 orders of magnitude higher than the average permeabilities of pillow hand-specimens. These results pertain to spilitized outcrops, yet the overlap of rock-matrix values for fresh and low-temperature altered basalts (Figures 7 and 8) suggest their upscaled values may be similar. Our upscaled results explain the discrepancy between the hand sample and the minimum in situ measurements, and are most relevant for high temperature, near-axis systems. However, they also suggest that attainment of crustal scale permeabilities significantly higher than 10^{-16} m^2 require the presence of extensive breccia zones, cooling joints or fracture networks.

7. Summary and Conclusions

Our investigation has defined how rock-matrix porosities and permeabilities influence hydrothermal fluid circulation though the spilitized and epidotized upper oceanic crust, as abundantly exposed in axial MORB-like lavas in the Semail ophiolite. The study has assessed the rock-matrix porosity and permeability by carefully avoiding or correcting the effects of processes that postdate the hydrothermal alteration of interest.

The porosity and permeability of basalts altered to prehnite–pumpellyite and greenschist-facies spilite assemblages correlate systematically with the igneous textures of their fresh basalt precursors. Thus, the original differences in crystal size, vesicularity and glass content between the various morphologies of basalt produce the following order of decreasing porosity and permeability:

$$\text{interpillow hyaloclastites} > \text{pillow cores} > \text{pillow rims} > \text{massive flows} \geq \text{dikes.}$$

The bulk permeability of the pillow lavas is strongly influenced by the highly permeable interpillow hyaloclastites. Their presence as a continuous 3D network through the pillow lavas renders the permeability of the lavas virtually anisotropic at the 10^4 m^3 scale. Nevertheless, the remaining pillow cores and rims have competitive permeabilities, such that the above order of decreasing permeabilities is followed during progressive alteration of spilite pillow stacks to epidosites, via the *incipient*, *intermediate* and *complete* stages documented by Gilgen et al. (2016). The reaction stoichiometry and molar volumes of the phases involved in the spilite-to-epidosite transformation generates up to 9–14 vol.% of new porosity and enhances the permeability of pillow lavas, massive lavas and dikes by up to 4 orders of magnitude, reaching $\sim 10^{-14}$ m^2 or perhaps even higher. The feedback of this enhancement on fluid flux through the rock-matrix explains the formation of km^3-size bodies of pervasive epidosites (Gilgen et al., 2016) in the absence of significant fracture networks. Moreover, this positive feedback mechanism facilitates the huge water–rock ratios (Weber et al., 2021) needed to quantitatively leach Mg and Na and form endmember epidosites.

The bulk porosities and permeabilities of prehnite–pumpellyite and greenschist-facies spilites are surprisingly similar to those of fresh basalts and low temperature clay-altered basalts in in situ oceanic crust, despite their mineralogical differences. Moreover, their porosity–permeability correlations are broadly comparable. Additionally, the results of hydraulic tests in pillow lavas in in situ upper crust can be reconciled with the rock-matrix permeabilities by combining the permeable network of interpillow hyaloclastites with pillow interiors, yielding a bulk pillow stack permeability of up to $\sim 10^{-16}$ m^2. This implies that the minimum permeabilities of $\sim 10^{-16}$ m^2 required to numerically simulate the observed heat flow and fluid discharge in near-axis seafloor settings may reflect a strong component of flow through the volcanic rock-matrix.

Our upscaled rock-matrix results at the 10^4 m^3 scale are suitable for use in future thermal–hydraulic–chemical modeling of both the volcanic crust and the sheeted dike complex, but a full assessment of bulk permeability still requires quantitative consideration of fracture networks. The present results provide a basis for a forthcoming study that combines our rock-matrix permeabilities with newly mapped fracture distributions in the Semail ophiolite, to evaluate their combined effect on the permeability of the extrusive sequence of the upper oceanic crust.

Data Availability Statement

All data on which this research is based are publicly available at the Zenodo repository (https://doi.org/10.5281/zenodo.6627013).

References

Alabaster, T., & Pearce, J. (1985). The interrelationship between magmatic and ore-forming hydrothermal processes in the Oman ophiolite. *Economic Geology*, *80*, 1–16. https://doi.org/10.2113/gsecongeo.80.1.1

Alabaster, T., Pearce, J. A., & Malpas, J. (1982). The volcanic stratigraphy and petrogenesis of the Oman ophiolite complex. *Contributions to Mineralogy and Petrology*, *81*(3), 168–183. https://doi.org/10.1007/BF00371294

Alt, J. C. (1995). Subseafloor processes in mid-ocean ridge hydrothermal systems. *Geophysical Monograph*, *91*, 85–114. https://doi.org/10.1029/GM091p0085

Anderson, R. N., Zoback, D. M., Hickman, S. H., & Newmark, R. L. (1985). Permeability versus depth in the upper oceanic crust: In situ measurements in DSDP hole 504B, eastern equatorial Pacific. *Journal of Geophysical Research*, *90*(B5), 3659–3669. https://doi.org/10.1029/JB090iB05p03659

Bach, W., Humphris, S. E., & Fisher, A. T. (2004). Fluid flow and fluid-rock interaction within ocean crust: Reconciling geochemical, geological, and geophysical observations. In W. S. D. Wilcock, E. F. DeLong, D. S. Kelley, J. A. Baross, & S. C. Cary (Eds.), *Subseafloor biosphere at mid-ocean ridges*. AGU.

Becker, K. (1989). Measurements of the permeability of the sheeted dikes in Hole 504B, ODP Leg 111. *Proceedings of the Ocean Drilling Program, Scientific Results*, *111*, 317–325. https://doi.org/10.2973/odp.proc.sr.111.156.1989

Becker, K., & Davis, E. E. (2003). New evidence for age variation and scale effects of permeabilities of young oceanic crust from borehole thermal and pressure measurements. *Earth and Planetary Science Letters*, *210*(3–4), 499–508. https://doi.org/10.1016/S0012-821X(03)00160-2

Becker, K., & Fisher, A. T. (2000). Permeability of upper oceanic basement on the eastern flank of the Juan de Fuca Ridge determined with drill-string packer experiments. *Journal of Geophysical Research*, *105*(B1), 897–912. https://doi.org/10.1029/1999JB900250

Belgrano, T. M., & Diamond, L. W. (2019). Subduction-zone contributions to axial volcanism in the Oman-U.A.E. ophiolite. *Lithosphere*, *11*(3), 399–411. https://doi.org/10.1130/L1045.1

Belgrano, T. M., Diamond, L. W., Novakovic, N., Hewson, R. D., Hecker, C. A., Wolf, R. C., et al. (2022). Multispectral discrimination of spectrally similar hydrothermal minerals in mafic crust: A 5000 km^2 ASTER alteration map of the Oman–UAE ophiolite. *Remote Sensing of Environment*, *280*, 113211. in press.

Belgrano, T. M., Diamond, L. W., Vogt, Y., Biedermann, A. R., Gilgen, S. A., & Al-Tobi, K. (2019). A revised map of volcanic units in the Oman ophiolite: Insights into the architecture of an oceanic proto-arc volcanic sequence. *Solid Earth*, *10*(4), 1181–1217. https://doi.org/10.5194/se-10-1181-2019

Belgrano, T. M., Tollan, P. M., Marxer, F., & Diamond, L. W. (2021). Paleobathymetry of submarine lavas in the Samail and Troodos ophiolites: Insights from volatiles in glasses and implications for hydrothermal systems. *Journal of Geophysical Research: Solid Earth*, *126*(7), e2021JB021966. https://doi.org/10.1029/2021JB021966

Brett-Adams, A. C., Diamond, L. W., Petrini, C., & Madonna, C. (2021). Influence of in-situ temperatures and pressures on the permeability of hydrothermally altered basalts in the oceanic crust. *Tectonophysics*, *815*, 228994. https://doi.org/10.1016/j.tecto.2021.228994

Cann, J. R., Mccaig, A. M., & Yardley, B. W. D. (2014). Rapid generation of reaction permeability in the roots of black smoker systems, Troodos ophiolite, Cyprus. *Geofluids*, *15*(1–2), 179–192. https://doi.org/10.1111/gfl.12117

Christensen, N. I., & Ramananantoandro, R. (1988). Permeability of the oceanic crust based on experimental studies of basalt permeability at elevated pressures. *Tectonophysics*, *149*(1–2), 181–186. https://doi.org/10.1016/0040-1951(88)90126-6

Christensen, N. I., & Smewing, J. D. (1981). Geology and seismic structure of the northern section of the Oman ophiolite. *Journal of Geophysical Research*, *86*(B4), 2545–2555. https://doi.org/10.1029/JB086iB04p02545

Coelho, G., Branquet, Y., Sizaret, S., Arbaret, L., Champallier, R., & Rozenbaum, O. (2015). Permeability of sheeted dykes beneath oceanic ridges: Strain experiments coupled with 3D numerical modeling of the Troodos Ophiolite, Cyprus. *Tectonophysics*, *644*, 138–150. https://doi.org/10.1016/j.tecto.2015.01.004

Coogan, L. A., & Gillis, K. M. (2018). Low-temperature alteration of the seafloor: Impacts on ocean chemistry. *Annual Review of Earth and Planetary Sciences*, *46*(1), 21–45. https://doi.org/10.1146/annurev-earth-082517-010027

Davis, E. E., & Becker, K. (2002). Observations of natural-state fluid pressures and temperatures in young oceanic crust and inferences regarding hydrothermal circulation. *Earth and Planetary Science Letters*, *204*(1–2), 231–248. https://doi.org/10.1016/S0012-821X(02)00982-2

Einaudi, F., Pezard, P. A., Cochemé, J.-J., Coulon, C., Laverne, C., & Godard, M. (2000). Petrography, geochemistry and physical properties of a continuous extrusive section from the Sarami Massif, Semail ophiolite. *Marine Geophysical Researches*, *21*, 387–407. https://doi.org/10.1023/A:1026752415989

Feig, S. T., Koepke, J., & Snow, J. E. (2006). Effect of water on tholeiitic basalt phase equilibria: An experimental study under oxidizing conditions. *Contributions to Mineralogy and Petrology*, *152*(5), 611–638. https://doi.org/10.1007/s00410-006-0123-2

Filomena, C. M., Hornung, J., & Stollhofen, H. (2014). Assessing accuracy of gas-driven permeability measurements: A comparative study of diverse Hassler-cell and probe permeameter devices. *Solid Earth*, *5*, 1–11. https://doi.org/10.5194/se-5-1-2014

Fisher, A. T. (1998). Permeability within basaltic ocean crust. *Reviews of Geophysics*, *36*(2), 143–182. https://doi.org/10.1029/97RG02916

Galley, A. G., Bailes, A. H., & Kitzler, G. (1993). Geological setting and hydrothermal evolution of the Chisel Lake and North Chisel Zn-Pb-Cu-Ag-Au massive sulfide deposits, Snow Lake, Manitoba. *Exploration And Mining Geology*, *2*, 271–295.

Gilbert, L. A., & Bona, M. L. (2016). Permeability of oceanic crustal rock samples from IODP Hole 1256D. *Geochemistry, Geophysics, Geosystems*, *17*(9), 3825–3832. https://doi.org/10.1002/2016GC006467

Gilbert, L. A., & Salisbury, M. H. (2011). Oceanic crustal velocities from laboratory and logging measurements of Integrated Ocean Drilling Program Hole 1256D. *Geochemistry, Geophysics, Geosystems*, *12*(9), Q09001. https://doi.org/10.1029/2011GC003750

Gilgen, S. A., Diamond, L. W., & Mercolli, I. (2016). Sub-seafloor epidosite alteration: Timing, depth and stratigraphic distribution in the Semail Ophiolite, Oman. *Lithos*, *260*, 191–210. https://doi.org/10.1016/j.lithos.2016.05.014

Gilgen, S. A., Diamond, L. W., Mercolli, I., Al-Tobi, K., Maidment, D. W., Close, R., & Al-Towaya, A. (2014). Volcanostratigraphic controls on the occurrence of massive sulfide deposits in the Semail Ophiolite, Oman. *Economic Geology*, *109*(6), 1585–1610. https://doi.org/10.2113/econgeo.109.6.1585

Gillis, K. M., & Banerjee, N. R. (2000). Hydrothermal alteration patterns in supra-subduction zone ophiolites. *Special Papers-Geological Society of America*, *349*, 283–298. https://doi.org/10.1130/0-8137-2349-3.283

Gillis, K. M., & Sapp, K. (1997). Distribution of porosity in a section of upper oceanic crust exposed in the Troodos Ophiolite. *Journal of Geophysical Research*, *102*(B5), 10133–10149. https://doi.org/10.1029/96JB03909

Guilmette, C., Smit, M. A., van Hinsbergen, D. J. J., Gürer, D., Corfu, F., Charette, B., et al. (2018). Forced subduction initiation recorded in the sole and crust of the Semail Ophiolite of Oman. *Nature Geoscience*, *11*(9), 688–695. https://doi.org/10.1038/s41561-018-0209-2

Hamano, Y. (1980). Physical properties of basalts from Holes 417D and 418A. *Initial Reports of the Deep Sea Drilling Project*, *51–53*, 1457–1466. https://doi.org/10.2973/dsdp.proc.515253.166.1980

Hannington, M. D. (2014). Volcanogenic massive sulfide deposits. In H. D. Holland & K. K. Turekian (Eds.), *Treatise on Geochemistry* (2nd ed., pp. 463–488). Elsevier.

Hannington, M. D., Santaguida, F., Kjarsgaard, I. M., & Cathles, L. M. (2003). Regional-scale hydrothermal alteration in the Central Blake River Group, western Abitibi subprovince, Canada: Implications for VMS prospectivity. *Mineralium Deposita*, *38*(4), 393–422. https://doi.org/10.1007/s00126-002-0298-z

Harper, G. D., Bowman, J. R., & Kuhns, R. (1988). A field, chemical, and stable isotope study of subseafloor metamorphism of the Josephine Ophiolite, California-Oregon. *Journal of Geophysical Research*, *93*(B5), 4625–4656. https://doi.org/10.1029/jb093ib05p04625

Hasenclever, J., Theissen-Krah, S., Rüpke, L. H., Morgan, J. P., Iyer, K., Petersen, S., & Devey, C. W. (2014). Hybrid shallow on-axis and deep off-axis hydrothermal circulation at fast-spreading ridges. *Nature*, *508*(7497), 508–512. https://doi.org/10.1038/nature13174

Jarrard, R. D., Abrams, L. J., Pockalny, R., Larson, R. L., & Hirono, T. (2003). Physical properties of upper oceanic crust: Ocean Drilling Program Hole 801C and the waning of hydrothermal circulation. *Journal of Geophysical Research: Solid Earth*, *108*(B4), 2188. https://doi.org/10.1029/2001JB001727

Johnson, D. M. (1980a). Crack distribution in the upper crust and its effects upon seismic velocity, seismic structure, formation permeability and fluid circulation. *Initial Reports of the Deep Sea Drilling Project*, *51–53*, 1457–1466. https://doi.org/10.2973/DSDP.PROC.515253.169.1980

Johnson, D. M. (1980b). Fluid permeability of oceanic basalts. *Initial Reports of the Deep Sea Drilling Project*, *68*, 1473–1477.

Jowitt, S. M., Jenkin, G. R. T., Coogan, L. A., & Naden, J. (2012). Quantifying the release of base metals from source rocks for volcanogenic massive sulfide deposits: Effects of protolith composition and alteration mineralogy. *Journal of Geochemical Exploration*, *118*, 47–59. https://doi.org/10.1016/j.gexplo.2012.04.005

Karato, S. (1983). Physical properties of basalts from Deep Sea Drilling Project Hole 504B, Costa Rica Rift. *Initial Reports of the Deep Sea Drilling Project*, *69*, 687–695. https://doi.org/10.2973/dsdp.proc.69.143.1983

Kusano, Y., Hayashi, M., Yoshiko, A., Umino, S., & Miyashita, S. (2014). Evolution of volcanism and magmatism during initial arc stage: Constraints on the tectonic setting of the Oman ophiolite. *Geological Society, London, Special Publications*, *392*(1), 177–193. https://doi.org/10.1144/SP392.9

Kusano, Y., Umino, S., Shinjo, R., Ikei, A., Adachi, Y., Miyashita, S., & Arai, S. (2017). Contribution of slab-derived fluid and sedimentary melt in the incipient arc magmas with development of the paleo-arc in the Oman Ophiolite. *Chemical Geology*, *449*, 206–225. https://doi.org/10.1016/j.chemgeo.2016.12.012

Lanari, P., Vho, A., Bovay, T., Airaghi, L., & Centrella, S. (2018). Quantitative compositional mapping of mineral phases by electron probe microanalyser. *Geological Society of London Special Publications*, *478*(1), 39–63. https://doi.org/10.1144/SP478.4

Lichtner, P. C. (2007). *FLOTRAN User's manual: Two-phase nonisothermal coupled thermal hydrologic-chemical (THC) reactive flow and transport code, version 2*. Los Alamos National Laboratory.

MacLeod, C. J., Lissenberg, J. C., & Bibby, L. E. (2013). "Moist MORB" axial magmatism in the Oman ophiolite: The evidence against a mid-ocean ridge origin. *Geology*, *41*(4), 459–462. https://doi.org/10.1130/G33904.1

Miyashita, S., Adachi, Y., & Umino, S. (2003). Along-axis magmatic system in the northern Oman ophiolite: Implications of compositional variation of the sheeted dike complex. *Geochemistry, Geophysics, Geosystems*, *4*(9), 8617. https://doi.org/10.1029/2001GC000235

Nehlig, P. (1994). Fracture and permeability analysis in magma-hydrothermal transition zones in the Samail ophiolite (Oman). *Journal of Geophysical Research*, *99*(B1), 589–601. https://doi.org/10.1029/93jb02569

Nehlig, P., Juteau, T., Bendel, V., & Cotten, J. (1994). The root zones of oceanic hydrothermal systems: Constraints from the Samail ophiolite (Oman). *Journal of Geophysical Research*, *99*(B3), 4703–4713. https://doi.org/10.1029/93JB02663

Nicolas, A., Boudier, F., Ildefonse, B., & Ball, E. (2000). Accretion of Oman and United Arab Emirates ophiolite – Discussion of a new structural map. *Marine Geophysical Researches*, *21*(3/4), 147–180. https://doi.org/10.1023/A:1026769727917

Patten, C. G. C., Pitcairn, I. K., Teagle, D. A. H., & Harris, M. (2016). Sulphide mineral evolution and metal mobility during alteration of the oceanic crust: Insights from ODP Hole 1256D. *Geochimica et Cosmochimica Acta*, *193*, 132–159. https://doi.org/10.1016/j.gca.2016.08.009

Pearce, J. A., Lippard, S. J., & Roberts, S. (1984). Characteristics and tectonic significance of supra-subduction zone ophiolites. In B. P. Kokelaar & M. F. Howells (Eds.), *Marginal Basin Geology: Volcanic and associated sedimentary and tectonic processes in modern and ancient marginal basins* (Vol. 16, pp. 77–94). Geological Society, London, Special Publications. https://doi.org/10.1144/GSL.SP.1984.016.01.06

Peters, D., & Pettke, T. (2016). Evaluation of major to ultra trace element bulk rock chemical analysis of nanoparticulate pressed powder pellets by LA-ICP-MS. *Geostandards and Geoanalytical Research*, *41*(1), 5–28. https://doi.org/10.1111/ggr.12125

Pezard, P. A. (1990). Electrical properties of mid-oceanic ridge basalt and implication for the structure of the upper oceanic crust in Hole 504B. *Journal of Geophysical Research*, *95*(B6), 9237–9264. https://doi.org/10.1029/JB095iB06p09237

Price, A. N., Fisher, A. T., Stauffer, P. H., & Gable, C. W. (2022). Numerical simulation of cool hydrothermal processes in the upper volcanic crust beneath a marine sediment pond: North Pond, North Atlantic Ocean. *Journal of Geophysical Research: Solid Earth*, *127*(1), e2021JB023158. https://doi.org/10.1029/2021JB023158

Richardson, C. J., Cann, J. R., Richards, H. G., Cowan, J. G., & Siegel, J. (1987). Metal-depleted root zones of the Troodos ore-forming hydrothermal systems, Cyprus. *Earth and Planetary Science Letters*, *84*(2–3), 243–253. https://doi.org/10.1016/0012-821x(87)90089-6

Richter, L., & Diamond, L. W. (2022). Characterization of hydrothermal fluids that alter the upper oceanic crust to spilite and epidosite: Fluid inclusion evidence from the Semail (Oman) and Troodos (Cyprus) ophiolites. *Geochimica et Cosmochimica Acta*, *39*, 220–253. https://doi.org/10.1016/j.gca.2021.11.012

Rioux, M., Benoit, M., Amri, I., Ceuleneer, G., Garber, J. M., Searle, M., & Leal, K. (2021). The origin of felsic intrusions within the mantle section of the Samail ophiolite: Geochemical evidence for three distinct mixing and fractionation trends. *Journal of Geophysical Research: Solid Earth*, *126*(5), e2020JB020760. https://doi.org/10.1029/2020JB020760

Seyfried, W. E., Mottl, M. J., & Bischoff, J. L. (1978). Seawater/basalt ratio effects on the chemistry and mineralogy of spilites from the ocean floor. *Nature*, *275*(5677), 211–213. https://doi.org/10.1038/275211a0

Staudigel, H. (2014). Chemical fluxes from hydrothermal alteration of the oceanic crust. In H. D. Holland & K. K. Turekian (Eds.), *Treatise on Geochemistry* (2nd ed., Vol. 4, pp. 583–603). Elsevier. https://doi.org/10.1016/B978-0-08-095975-7.00318-1

Tominaga, M., Teagle, D. A. H., Alt, J. C., & Umino, S. (2009). Determination of the volcanostratigraphy of oceanic crust formed at superfast spreading ridge: Electrofacies analyses of ODP/IODP Hole 1256D. *Geochemistry, Geophysics, Geosystems*, *10*, 1–31. https://doi.org/10.1029/2008GC002143

van Everdingen, D. A. (1995). Fracture characteristics of the sheeted dike complex, Troodos ophiolite, Cyprus: Implications for permeability of oceanic crust. *Journal of Geophysical Research*, *100*(B10), 19957–19972. https://doi.org/10.1029/95JB01575

Violay, M., Pezard, P. A., Ildefonse, B., Belghoul, A., & Laverne, C. (2010). Petrophysical properties of the root zone of sheeted dikes in the ocean crust: A case study from hole ODP/IODP 1256D, Eastern Equatorial Pacific. *Tectonophysics*, *493*(1–2), 139–152. https://doi.org/10.1016/j.tecto.2010.07.013

Weber, S., Diamond, L. W., Alt-Epping, P., & Brett-Adams, A. C. (2021). Reaction mechanism and water/rock ratios involved in epidosite alteration of the oceanic crust. *Journal of Geophysical Research: Solid Earth*, *126*(6), e2020JB021540. https://doi.org/10.1029/2020JB021540

References From the Supporting Information

Kusano, Y., Adachi, Y., Miyashita, S., & Umino, S. (2012). Lava accretion system around mid-ocean ridges: Volcanic stratigraphy in the Wadi Fizh area, northern Oman ophiolite. *Geochemistry, Geophysics, Geosystems*, *13*, Q05012. https://doi.org/10.1029/2011GC004006